Open access • Journal Article • DOI:10.1088/0004-637X/804/2/81

Constraining the Abundances of Complex Organics in the Inner Regions of Solar-type Protostars — Source link

Vianney Taquet, Vianney Taquet, Ana López-Sepulcre, Ana López-Sepulcre ...+7 more authors

Institutions: Leiden University, Goddard Space Flight Center, Centre national de la recherche scientifique, University of Grenoble ...+1 more institutions

Published on: 05 May 2015 - The Astrophysical Journal (IOP Publishing)

Topics: Plateau de Bure Interferometer

The Astrophysical Journal, 804:81 (30pp), 2015 May 10 doi:10.1088/0004-637X/804/2/81

CONSTRAINING THE ABUNDANCES OF COMPLEX ORGANICS IN THE INNER REGIONS OF SOLAR-TYPE PROTOSTARS

Vianney Taquet[1,2,7], Ana López-Sepulcre[3,4,5], Cecilia Ceccarelli[3,4], Roberto Neri[6], Claudine Kahane[3,4], and Steven B. Charnley[1]

[1] Astrochemistry Laboratory and The Goddard Center for Astrobiology, Mailstop 691, NASA Goddard Space Flight Center, 8800 Greenbelt Road, Greenbelt, MD 20770, USA; taquet@strw.leidenuniv.nl
[2] Leiden Observatory, Leiden University, P.O. Box 9513, 2300-RA Leiden, The Netherlands
[3] Univ. Grenoble Alpes, IPAG, F-38000 Grenoble, France
[4] CNRS, IPAG, F-38000 Grenoble, France
[5] Department of Physics, The University of Tokyo, Bunkyo-ku, Tokyo 113-0033, Japan
[6] Institut de Radioastronomie Millimétrique, Grenoble, France
Received 2014 October 31; accepted 2015 February 23; published 2015 May 5

ABSTRACT

The high abundances of Complex Organic Molecules (COMs) with respect to methanol, the most abundant COM, detected toward low-mass protostars, tend to be underpredicted by astrochemical models. This discrepancy might come from the large beam of the single-dish telescopes, encompassing several components of the studied protostar, commonly used to detect COMs. To address this issue, we have carried out multi-line observations of methanol and several COMs toward the two low-mass protostars NGC 1333-IRAS 2A and -IRAS 4A with the Plateau de Bure interferometer at an angular resolution of 2″, resulting in the first multi-line detection of the O-bearing species glycolaldehyde and ethanol and of the N-bearing species ethyl cyanide toward low-mass protostars other than IRAS 16293. The high number of detected transitions from COMs (more than 40 methanol transitions for instance) allowed us to accurately derive the source size of their emission and the COM column densities. The COM abundances with respect to methanol derived toward IRAS 2A and IRAS 4A are slightly, but not substantitally, lower than those derived from previous single-dish observations. The COM abundance ratios do not vary significantly with the protostellar luminosity, over five orders of magnitude, implying that low-mass hot corinos are quite chemically rich as high-mass hot cores. Astrochemical models still underpredict the abundances of key COMs, such as methyl formate or di-methyl ether, suggesting that our understanding of their formation remains incomplete.

Key words: astrochemistry – ISM: abundances – ISM: individual objects (NGC 1333-IRAS 2A, NGC 1333-IRAS 4A) – ISM: molecules – stars: formation

1. INTRODUCTION

The early stages of low-mass star formation are known to be accompanied by the increase of the molecular complexity. Most of the lines detected in the sub-millimetric spectra of Class 0 protostars are attributed to Complex Organic Molecules (COMs, i.e., molecules based on carbon chemistry with six or more atoms; Herbst & van Dishoeck 2009), as shown by unbiased spectral surveys of low-mass protostars (see Caux et al. 2011 for the spectral survey of the low-mass protostar IRAS 16293-2422 for instance).

The bright protostars IRAS 16293-2422 and NGC 1333-IRAS 4A (hereafter IRAS 16293 and IRAS 4A, respectively) have been the first two protostars where COMs, such as methyl formate, di-methyl ether, formic acid, methyl cyanide, or ethyl cyanide, have been detected with single-dish telescopes (Cazaux et al. 2003; Bottinelli et al. 2004a). The subsequent detection of a few COMs toward IRAS 16293 with interferometers, providing better angular resolutions of ∼2″, by Bottinelli et al. (2004b) and Kuan et al. (2004) confirmed that most of the COM emission likely comes from the warm inner region of protostellar envelopes, called "hot corinos": the low-mass counterparts of high-mass hot cores. Since then, the number of low-mass protostars showing COMs has increased with the detection of COMs toward ∼10 other low-mass protostars by Bottinelli et al. (2007) and Öberg et al. (2011, 2014). Palau et al. (2011) and Fuente et al. (2014) also reported the detection of several COMs toward four low/intermediate-mass protostars.

Thanks to a larger number of transitions detected in the broad bands of their receivers, single-dish telescopes have been first used to derive the column densities of COMs, allowing them to constrain their abundances averaged over a relatively large beam of 10″–30″. The abundances of COMs, usually compared to that of their probable mother molecules (formaldehyde and methanol; see next paragraph), are found to be relatively high: $\gtrsim$10% for methyl formate, di-methyl ether, and formic acid, and ∼1% for methyl cyanide and ethyl cyanide (see Bottinelli et al. 2007; Öberg et al. 2011, 2014), although the number of constrained abundance ratios remains relatively low and the abundances show some scattering between the sources and molecules.

Warm gas phase chemistry triggered by the sublimation of the main ice components, and of methanol in particular, has been first invoked by Millar et al. (1991) and Charnley et al. (1992) to explain the presence of COMs observed toward the high-mass hot core Orion KL by Blake et al. (1987). However, more recent laboratory experiments and theoretical calculations have contradicted several key assumptions made in the gas phase models: dissociative recombination of large ions does not lead predominantly to the formation of COMs but rather to their fragmentation into small pieces (Geppert

[7] NASA Postdoctoral Program Fellow.

et al. 2006; Hamberg et al. 2010), while ion-molecule reactions have been found to be not sufficiently efficient to produce the observed amount of methyl formate (Horn et al. 2004). The current scenario of COM formation is now based on the recombination of radicals at the surface of interstellar grains during the warm-up phase ($30\,\mathrm{K} < T < 100\,\mathrm{K}$) occurring in the envelopes surrounding Class 0 protostars (Garrod & Herbst 2006; Garrod et al. 2008). In these models, the radicals are generated by the UV photodissocation of the main ice components, or they have survived to the incomplete hydrogenation process of CO leading to CH_3OH during the ice formation (Garrod & Herbst 2006; Taquet et al. 2012). Since the 1990 s, laboratory experiments have shown that UV irradiation of interstellar ice analogs containing methanol, formaldehyde, and ammonia can lead to the formation of a plethora of complex molecules and even amino acids (Allamandola et al. 1988; Gerakines et al. 1996; Hudson & Moore 2000; Muñoz Caro et al. 2002; Öberg et al. 2009). However, the quantitative efficiency of the COM formation in ices and their actual chemical pathways are still highly uncertain.

Although the current models produce a large set of COMs in significant quantities, they are not able to explain the very high abundance ratio (>10%) with respect to methanol seen for a few COMs, such as methyl formate or di-methyl ether (see Taquet et al. 2012 for a discussion of this problem). The discrepancy between observations and models could be due to the large beams of single-dish telescopes used to derive the abundance ratios of COMs. Typical single-dish beams of $\sim 10''$ are much larger than the size of hot corinos ($\sim 0.5''$; Maret et al. 2005; Maury et al. 2014) and encompass the cold envelopes and possible outflows driven by the central protostars, where COMs have also been detected (Arce et al. 2008; Öberg et al. 2010; Jaber et al. 2014). In addition, COMs have also been found in cold and quiescent cores by Bacmann et al. (2012) and Cernicharo et al. (2012), who claimed that quiescent cold gas phase chemistry can produce COMs but in lower quantities. However, new observations by Vastel et al. (2014) rather suggest that the emission from COMs observed in another pre-stellar core originates in an outer ring, so that the previous conclusions may need some cautions.

To better constrain the abundances of COMs originating from the hot corinos surrounding the low-mass protostars, a large number of transitions of methanol and COMs need to be observed with interferometers, providing angular resolutions of $\sim 1''$–$2''$. The emission originating from hot corinos can be distinguished from other components of the envelope, allowing us to directly derive the abundance of COMs in the hot corinos. Moreover, CH_3OH emission is likely optically thick toward the continuum peak of protostars (Zapata et al. 2013); observations of its optically thin isotopologue $^{13}CH_3OH$ are therefore required to derive an accurate estimate of the methanol column density. Although several publications have reported the interferometric detection of COMs in hot corinos (Bottinelli et al. 2004b; Kuan et al. 2004; Jørgensen et al. 2005; Bisschop et al. 2008; Jørgensen et al. 2011, 2012; Persson et al. 2012; Maury et al. 2014), to our knowledge, none of them led to an accurate and simultaneous estimation of the column densities of methanol and COMs.

In this work, we present multi-line observations of methanol ($^{12}CH_3OH$, and $^{13}CH_3OH$) as well as several COMs (methyl formate, di-methyl ether, ethanol, glycolaldehyde methyl cyanide, and ethyl cyanide) performed with the Plateau de Bure interferometer (PdBi) toward the two low-mass protostars IRAS 2A and IRAS 4A located in the NGC 1333 star-forming region. Although the angular resolution does not allow us to spatially resolve the emission of COMs, it is sufficiently high to distinguish the emission from the hot corinos from other components of protostellar envelopes. The paper is structured as follows: Section 2 describes the observational strategy, Section 3 presents the continuum maps as well as the spectra and the maps of molecular transitions, Section 4 explains the adopted methodology to derive the abundances of COMs, Section 5 discusses the results, and Section 6 summarizes this work with the conclusions.

2. OBSERVATIONS

The two low-mass Class 0 protostars IRAS 2A and IRAS 4A were observed with the IRAM PdBi on 2010 July 20, July 21, August 1, August 3, November 24, and 2011 March 10 in the C and D configurations of the array. Due to the proximity to each other, the two sources were observed in the same track. Phase and amplitude were calibrated by performing regular observations of the nearby point sources 3C 454.3, 3C 84, and 0333+321. The amplitude calibration uncertainty is estimated to be ∼20%. The WIDEX backends have been used at 143.4 and 165.2 GHz, providing a bandwidth of 3.6 GHz each with a spectral resolution of 1.95 MHz (~ 3.5–$4\,\mathrm{km\,s^{-1}}$). High-resolution narrowband backends focused on two CH_3OH lines and 12 $HCOOCH_3$ lines have also been used. They provide a bandwidth of 80 MHz with a spectral resolution of 0.04 MHz ($0.08\,\mathrm{km\,s^{-1}}$). Due to the low signal-to-noise ratio (S/N) obtained for the methyl formate lines at high spectral resolution, we decreased the spectral resolution to 0.4 MHz ($0.8\,\mathrm{km\,s^{-1}}$) to obtain an S/N higher than 3. The data calibration and imaging were performed using the CLIC and MAPPING packages of the GILDAS software.[8] Continuum images were produced by averaging line-free channels in the WIDEX correlator before the Fourier transformation of the data. The coordinates of the source and the size of the synthesized beams are reported in Table 1.

3. RESULTS

3.1. Continuum Maps

Figure 1 shows the maps of the continuum emission of IRAS 2A and IRAS 4A at 143 and 165 GHz obtained after natural weighted cleaning. Parameters of the continuum emission (integrated flux and deconvolved FWHM size), obtained from elliptical Gaussian fits in the (u, v) plane, are given in Table 1. For the two settings, the FWHM size of the continuum emission is slightly smaller than the size of the synthesized beam; the continuum emission is consequently not resolved. In particular, IRAS 4A is known to be a binary system with a $1\farcs8$ separation (Looney et al. 2000), as depicted by the two red crosses in Figure 1 that indicate the positions of IRAS 4A-SE and -NW. Although the continuum emission of IRAS 4A is

[8] http://www.iram.fr/IRAMFR/GILDAS

Table 1
Properties of NGC 1333 IRAS 2A and IRAS 4A

Parameters	IRAS 2A	IRAS 4A
R.A. (J2000)	03:28:55:57	SE: 03:29:10.52
	...	NW: 03:29:10.42
Decl. (J2000)	31:14:37:22	SE: 31:13:31.06
	...	NW: 31:13:32.04
d (pc)[a]	235	235
V_{LSR} (km s^{-1})	+7.7	+7.2
L_{bol} ($L_\odot$)[b]	36	9.1
M_{env} ($M_\odot$)[c]	5.1	5.6
Frequency = 143 GHz		
Beam size ($''$)	2.2 × 1.7	2.1 × 1.7
Beam PA (°)	25	25
rms(WideX)[d]	2.57	3.34
rms(Cont.)[e]	1.56	10.8
Flux (Jy)[f]	0.13	1.1
Size ($''$)[f]	1.7 × 1.7	2.1 × 1.7
PA (°)[f]	+51	+25
M ($M_\odot$)[g]	0.4	3.8
$N(H_2)$ (cm^{-2})[g]	5.0×10^{24}	3.7×10^{25}
Frequency = 165 GHz		
Beam size ($''$)	2.3 × 1.7	2.4 × 1.8
Beam PA (°)	110	115
rms(WideX)[d]	3.50	4.02
rms(Cont.)[e]	1.84	10.8
Flux (Jy)[f]	0.19	1.6
Size ($''$)[f]	1.9 × 1.7	2.5 × 1.6
PA (°)[f]	−67	-44
M ($M_\odot$)[g]	0.4	3.5
$N(H_2)$ (cm^{-2})[g]	4.5×10^{24}	3.1×10^{25}

Notes:
[a] Hirota et al. (2008).
[b] Karska et al. (2013).
[c] Kristensen et al. (2012).
[d] Units of mJy/beam/channel for a channel width of 1.95 MHz.
[e] Units of mJy/beam.
[f] Continuum integrated fluxes and sizes were obtained from elliptical. Gaussian fits in the (u, v) plane (i.e., deconvolved FWHM size).
[g] The envelope mass and averaged column density were derived from the continuum fluxes obtained within the deconvolved FWHM size (see text for more details).

peaked at the southeast (SE) position rather than at the northwest (NW) position for the two settings, we cannot resolve the two sources.

We estimated the mass of the envelope and the H_2 column density from the continuum fluxes and the sizes derived from elliptical Gaussian fits listed in Table 1. Assuming an optically thin dust emission, the mass M of the envelope is given by

$$M = \frac{S_\nu d^2}{K_\nu B_\nu(T_d) R_d}, \quad (1)$$

where S_ν is the continuum flux integrated over the Gaussian ellipse and listed in Table 1, d is the distance to the two low-mass protostars (235 pc; Hirota et al. 2008), $B_\nu(T_d)$ is the Planck blackbody function for a temperature T_d assumed to be 30 K, and R_d is the dust-to-gas mass ratio equal to 0.01. K_ν is the opacity per dust mass taken from column 5 in Table 5 of Ossenkopf & Henning (1994) (corresponding to grains showing an MRN size distribution covered by thin ice mantles at $n_H = 10^6$ cm^{-3}) and extrapolated to 145 GHz ($K_\nu = 0.38$ g cm^{-2}) and 165 GHz ($K_\nu = 0.48$ g cm^{-2}). The column density of H_2 averaged over the Gaussian ellipse can be deduced from M following this formula:

$$N(H_2) = \frac{M}{\mu m_H \Omega d^2}, \quad (2)$$

where M is the envelope mass, $\mu = 2.38$ is the mean molecular mass in units of hydrogen atom masses, m_H is the hydrogen atom mass, and Ω is the solid angle subtended by the Gaussian ellipse. The envelope mass M and H_2 column density $N(H_2)$ derived for the two frequencies are listed in Table 1.

3.2. Spectra

For the two sources and for all the settings, we obtained the spectral cubes by subtracting the continuum visibilities from the whole (line+continuum) datacube. For IRAS 4A, the baseline has been flattened by importing the data cubes into CLASS and subtracting a polynomial function to each individual spectrum. The 3.6 GHz wide spectra obtained at the coordinates of IRAS 2A and IRAS 4A-NW with the two WideX backends are presented in Figure 2. We also present the narrowband spectra of CH_3OH and $HCOOCH_3$ in Figures 3 and 4. The 1σ rms noise in the line-free channels of all spectra is given in the caption of Figures 2–4. The two sources are chemically rich since the WideX spectra toward IRAS 2A and IRAS 4A-NW display ~200 and ~170 lines detected with an S/N higher than 3, resulting in a line density of 28 and 23 detected lines per GHz, respectively. For comparison, Maury et al. (2014) detected 86 lines above the 3σ level between 216.9 and 220.5 GHz toward IRAS 2A with the PdBi, resulting in a similar line density of 24 detected lines per GHz.

The line identification was carried out using the JPL (Pickett et al. 1998) and the CDMS (Müller et al. 2005) spectroscopic catalogs. Line identifications were performed by eye, by taking into account the upper energy level, the line strength, and the velocity of each transition. The detected molecules are listed in Table 2 with the number of detected transitions, the energy range of their upper energy levels, and the spectroscopic reference. We detected about 35 transitions for the main isotopologue of methanol with upper energy levels up to ~1020 K and about 13 lines for its isotopologue $^{13}CH_3OH$. In addition to methanol, we report the first multi-line detection of glycol aldehyde $HCOCH_2OH$, ethyl cyanide C_2H_5CN, and ethanol C_2H_5OH toward low-mass protostars other than IRAS 16293.[9] We also detected several transitions originating from methyl formate $HCOOCH_3$, di-methyl ether CH_3OCH_3, and methyl cyanide CH_3CN toward the two sources. Due to the low spectral resolution, we carefully checked that the detected lines do not suffer from any blending with other transitions from similar or other

[9] The detection of glycolaldehyde was reported in IRAS 2A by Coutens et al. (2015) while this article was in the review process.

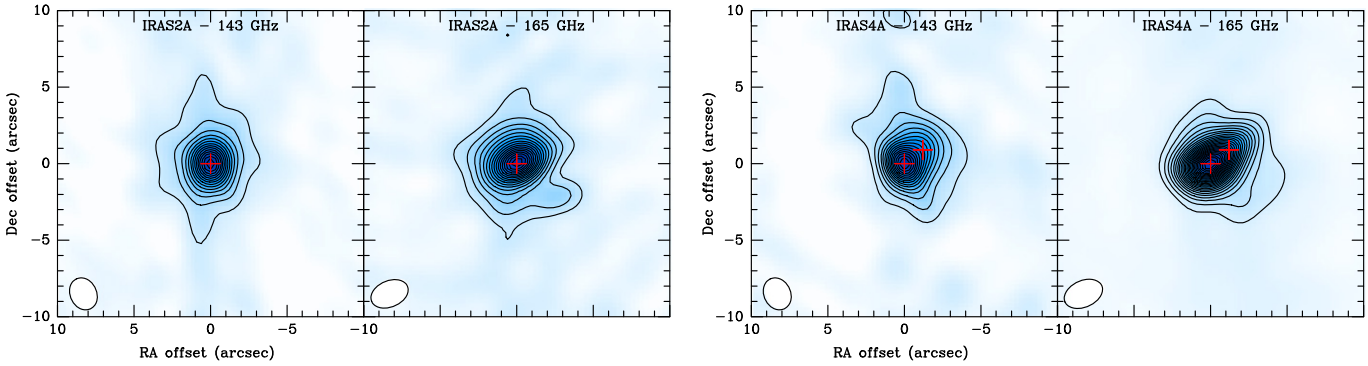

Figure 1. Continuum maps at 145 and 165 GHz of IRAS 2A (rms of 1.56 and 1.84 mJy beam^{-1}, respectively) and IRAS 4A (rms of 10.8 and 10.8 mJy beam^{-1}, respectively). The positions of the sources IRAS 2A, IRAS 4A-NW, and IRAS 4A-SE are marked by a red plus sign. Contour levels are in steps of 3σ. The white ellipse represents the half-power beamwidth of the synthesized beam.

molecules by using the JPL and CDMS databases but also with the Splatalogue database.[10] In total, about 70% of the lines detected at a 3σ level in the two 3.6 GHz WideX correlators are attributed to the complex organics listed in Table 2. Other lines are attributed to the deuterated methanol isotopologues CH_2DOH, CH_3OD, CHD_2OH, other deuterated molecules such as HDO (studied in a previous work; Taquet et al. 2013), DCN, NH_2D, and DCO^+ (in absorption), and the sulphur-bearing species SO_2, and $C^{34}S$. The analysis of the deuterated methanol transitions will be published in a separate article. Approximately 20 lines are unidentified.

We estimated the FWHM of the lines detected with the narrowband correlators giving a spectral resolution of 0.4 MHz, and with the WideX correlator providing a spectral resolution of 1.95 MHz, through a Gaussian fit of the spectra obtained at the coordinates of IRAS 2A and IRAS 4A-NW. Table 3 lists the line widths of the transitions detected with the two correlators. The uncertainties in the linewidths are due to the statistical errors from the Gaussian fit and to the uncertainty from the low spectral resolution. In this work, the low spectral resolution dominates the uncertainty of the linewidths. Tables A1–A9 of the Appendix list the properties of all detected transitions along with the FWHM linewidths. For the two sources, the FWHM of the CH_3OH transitions detected at high spectral resolution is about 3 km s^{-1}, while the widths of the $HCOOCH_3$ lines vary between 0.9 and 2.8 km s^{-1} when the lines of the -E and the -A states do not overlap. The linewidths derived with the PdBi are similar to the linewidths of other CH_3OH and $HCOOCH_3$ transitions derived by Maret et al. (2005) and Bottinelli et al. (2004a). Due to the low spectral resolution, the linewidths derived from the WideX correlators result from the convolution of the intrinsic linewidths with the spectral resolution of 1.95 MHz. The top panel of Figure 5 shows the deconvolved FWHM of CH_3OH, $^{13}CH_3OH$, $HCOOCH_3$, and CH_3CN, showing a high number of transitions detected at a high S/N, as a function of the energy of the upper level toward the two sources. For this purpose, we excluded several CH_3OH and $HCOOCH_3$ transitions that are blended with each other. No clear trend can be deduced for the two sources. The fluctuation of the deconvolved FWHM linewidths between 2 and 8 km s^{-1} seems to be due to their high uncertainties. The bottom panel of Figure 5 compares the linewidths deduced from the narrowband correlators giving a high spectral resolution of 0.4 MHz with the deconvolved linewidths from the WideX spectra for the lines detected with the narrowband correlators. For all the lines, the FWHM linewidth deconvolved from the WideX spectra is higher than the FWHM linewidth deduced from the narrowband correlator, but the differences remain within the uncertainties.

[10] http://www.cv.nrao.edu/php/splat/

3.3. Line Maps

For all the transitions, the interferometric maps of the IRAS 2A and IRAS 4A protostars have been obtained by integrating the flux over $V_{LSR} \pm \Delta V$, where V_{LSR} is the system velocity of the source and $\Delta V = 3$ km s^{-1} following the FWHM linewidths of the CH_3OH transitions listed in Table 3. In practice, due to the low resolution of the WideX backends, the line emission is integrated over three channels. Figures 6 and 7 show a compilation of the integrated line maps toward IRAS 2A and IRAS 4A obtained after natural weighted cleaning. For species where several transitions were detected, two maps showing a low-energy and a high-energy transition are presented. Tables A1–A9 of the Appendix list the properties of all detected transitions along with their FWHM sizes of emission and their position angle (PA) derived from the modeling of the visibilities assuming elliptical Gaussians, circular Gaussians, or point sources if Gaussian fits were not possible.

For the two sources, the emission of most molecules is limited to the inner regions near the protostars. In IRAS 4A, the compact emission of all COM transitions originates from the -NW source although the SE protostar is brighter in the continuum. In contrast, no molecular lines seem to originate from IRAS 4A-SE, as also observed in previous interferometric observations of $H_2^{18}O$ and other complex organics by Persson et al. (2012). The low-energy transitions of CH_3OH (the transition at ~145.094 GHz including several non-resolved transitions toward IRAS 2A not shown in this work and all the transitions with $E_{up} \leqslant 120$ K toward IRAS 4A) show an extended emission consistent with the position of molecular outflows. For IRAS 2A, the interferometric map of the CH_3OH transitions at ~145.094 GHz displays a slightly redshifted emission located 7″ to the north from IRAS 2A, consistent with the direction of an outflow previously

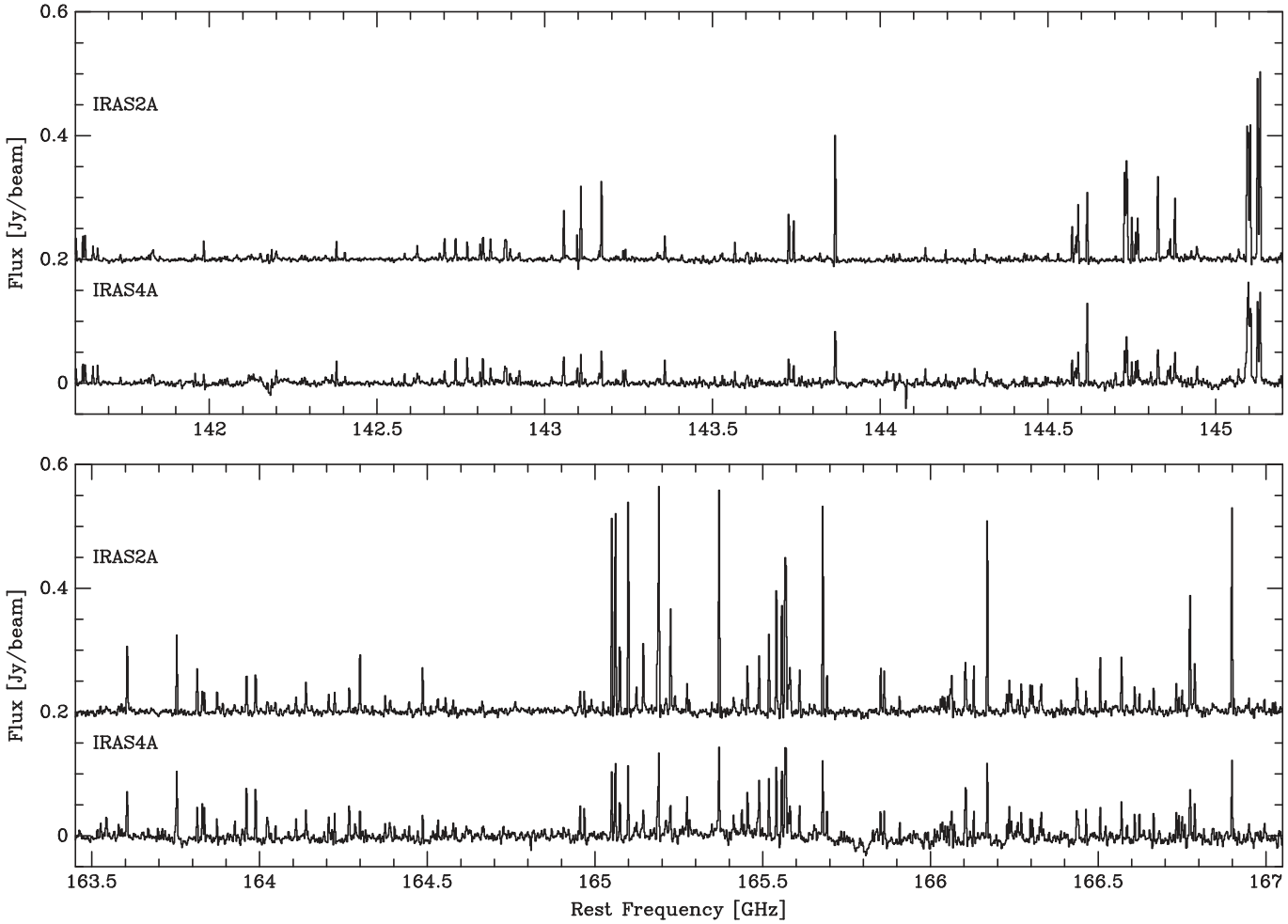

Figure 2. PdBi continuum-subtracted spectra of the WideX backends around 143 and 165 GHz toward the peak position of IRAS 2A and IRAS 4A-NW. The rms noise levels are 2.57 and 3.50 mJy/beam/channel at 143 and 165 GHz toward IRAS 2A and 3.34 and 4.02 mJy/beam/channel at 143 and 165 GHz toward IRAS 4A, respectively.

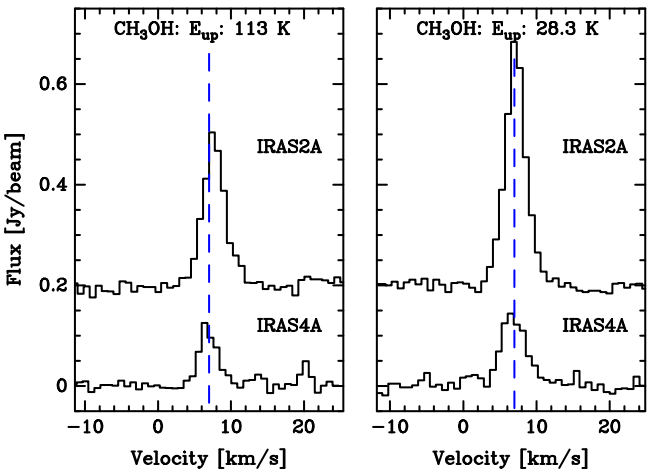

Figure 3. PdBi spectra of methanol obtained with the narrowband correlators toward the peak position of IRAS 2A and IRAS 4A-NW. The rms noise levels are 7.80 and 7.86 mJy/beam/channel toward IRAS 2A and IRAS 4A, respectively.

detected at small scales with CO by Jørgensen et al. (2007). For IRAS 4A, the emission of the low-energy CH_3OH lines extends in the bipolar outflow along an N-S direction and seems to peak at $\sim 10''$ south from the protostars, consistent with the south lobe detected in SiO by Choi (2005). From Figure 7, it is clear that the inner hot corino does not dominate the flux of the weakly excited transitions of methanol in IRAS 4A (see also Maret et al. 2005). The emission of the HC_3N transition is also spatially resolved and shows an elongation of its emission toward the SW direction for IRAS 2A and toward the N direction for IRAS 4A. The spatial distribution and the kinematics of the outflow driven by IRAS 2A and IRAS 4A will be analyzed in a future work.

The emission originating from all COM transitions except some CH_3OH and HC_3N lines is not spatially resolved by the array since their FWHM emission size deduced from the fit to the visibilities is lower than the synthesized beam of the interferometer. Consequently, the source sizes presented in this work can only be used as upper limits. These observations are qualitatively consistent with previous models and observations suggesting that methanol and COMs mostly come from the inner hot corino. In this region, these molecules show a jump of their abundance when the temperature is higher than the temperature of ice sublimation ($T \sim 100$ K). Maret et al. (2004) estimated a size for the hot corinos of IRAS 2A and IRAS 4A of $0''.45$ by reproducing the

formaldehyde emission observed with single-dish telescopes with an abundance jump of two orders of magnitude at $r \sim 50$ AU from the central protostar. The luminosities assumed for IRAS 2A and IRAS 4A by Maret et al. (2004) are lower by a factor of 2.25 and 1.5, respectively, than the luminosities assumed in this work. Assuming that the temperature profile is governed by the Stefan–Boltzmanns law implies a difference in the temperature of a factor of 1.2 and 1.1, respectively. The assumption of higher luminosities for the two sources would therefore increase the size of the corino by a few AU. Maury et al. (2014) estimated an FWHM size of 0.″4–0.″9 for the hot corino of IRAS 2A through the use of the more extended A configuration of the PdBi array.

4. CHEMICAL ABUNDANCES IN THE HOT CORINOS

4.1. Rotational Diagrams

First estimates of the excitation temperatures and the column densities of observed molecules in the hot corinos of IRAS 2A and IRAS 4A have been obtained from the rotational diagram (RD) analysis by assuming optically thin emission and an LTE population of the levels. Since the emission of most transitions is not spatially resolved with the PdBi, we measured the flux of all transitions originating from a circular mask with a diameter equal to the major axis of the synthesized beam size of the telescope (∼2.″1–2.″6). Tables A1–A9 of the Appendix list the measured flux for all transitions and in the two sources.Astrochemical/dynamical models predict low abundances of COMs in the the dense regions of protostellar envelopes where the dust temperature is lower than the temperature of ice sublimation T_{ev} (∼100 K) due to the efficient depletion, while the abundance profiles show a strong jump once $T = T_{ev}$ (see Aikawa et al. 2008; Taquet et al. 2014) induced by thermal evaporation in the hot corino. We therefore assumed that all the flux measured in the ∼2″ mask comes from the hot corino region. The emission sizes of the COMs are not necessarily similar, because of their different binding energies (see Jaber et al. 2014 for the example of IRAS 16293). Nevertheless, we assumed a same hot corino size θ_s of 0.″5 for all COMs. The linewidth at FWHM ΔV is fixed to 3 km s^{-1}, which represents an average value of Table 3 and previous observations by Maret et al. (2005) and Bottinelli et al. (2007). For molecules with only a few lines detected within a narrow range of upper energy levels (glycolaldehyde, or ethyl cyanide) or for molecules showing only one detection, we assumed two values for the rotational temperature T_{rot}: $T_{rot} = T_{rot}(CH_3OH)$ and $T_{rot} = T_{evap}(ice) = 100$ K. As already shown in several published observational works studying the emission of

Table 2
List of Molecules Detected toward IRAS 2A and IRAS 4A

Molecule	IRAS 2A		IRAS 4A		Ref.
	N_{lines}	E_{up} (K)	N_{lines}	E_{up} (K)	
CH_3OH	34	14–1022	35	14–1022	1
$HCOOCH_3$	20	43–248	20	43–237	2
CH_2DOH	13	33–230	13	33–230	3
$^{13}CH_3OH$	13	14–222	12	14–222	4
CH_3OCH_3	8	11–314	7	11–314	5
C_2H_5OH	8	37–216	7	37–216	6
CH_3CN	7	40–390	7	40–390	7
CHD_2OH	6	20–67	6	20–67	8
$HCOCH_2OH$	4	53–68	7	53–177	9
SO_2	4	24–102	4	24–102	10
C_2H_5CN	4	63–130	3	63–130	11
CH_3OD	1	40	1	40	12
$H_2^{13}CO$	1	10	1	10	13
$H_2C^{18}O$	1	22	1	22	14
HC_3N	1	75	1	75	15
NH_2CHO	1	30	1	30	16
CH_2CO	1	41	1	41	17
$C^{34}S$	1	14	1	14	18
DC_3N	1	62	…	…	15
HDO	1	319	1	319	19
DCN	1	10	1	10	20
NH_2D	1	183	1	183	21
D_2CO	1	21	1	21	14

References. (1) Xu et al. (2008), (2) Ilyushin et al. (2009), (3) Pearson et al. (2012), (4) Xu & Lovas (1997), (5) Lovas et al. (1979), (6) Endres et al. (2009), (7) Cazzoli & Puzzarini (2006), (8) Parise et al. (2002), (9) Carrol et al. (2010), (10) Alekseev et al. (1996), (11) Fukuyama et al. (1996), (12) Anderson et al. (1988), (13) Müller et al. (2000), (14) Dangoisse et al. (1978), (15) Lafferty & Lovas (1978), (16) Johnson et al. (1972), (17) Fabricant et al. (1977), (18) Bogey et al. (1982), (19) Messer et al. (1984), (20) De Lucia & Gordy (1969), (21) Cohen & Pickett (1982).

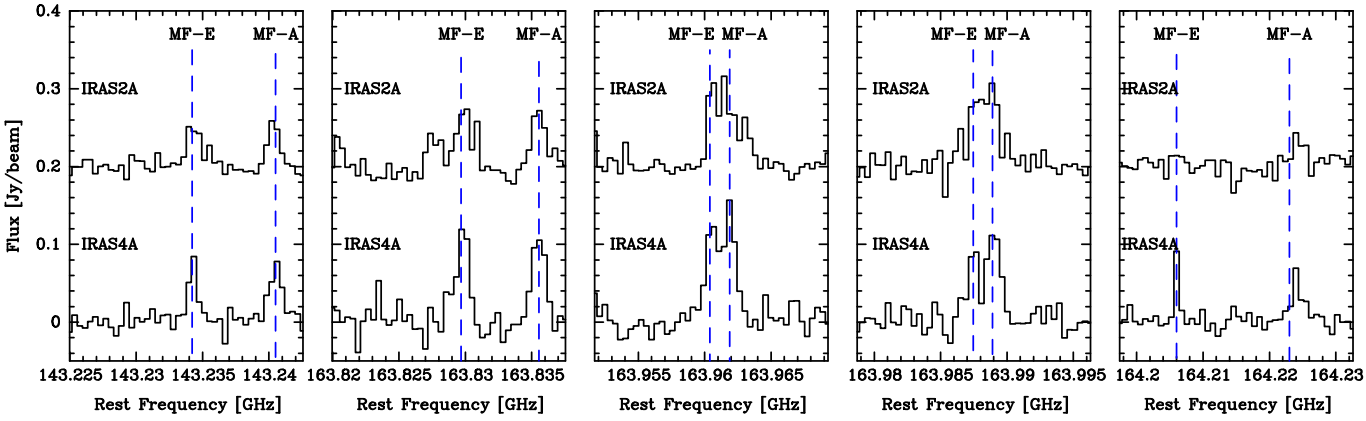

Figure 4. PdBi spectra of methyl formate obtained with the narrowband correlators toward the peak position of IRAS 2A and IRAS 4A-NW. The rms noises are about 7–10 mJy/beam/channel toward IRAS 2A and IRAS 4A.

Table 3
Line Widths of the Transitions Detected in the Narrowband Correlators

Molecule	Frequency (GHz)	E_{up} (K)	IRAS 2A		IRAS 4A	
			dV_n (km s^{-1})	dV_W (km s^{-1})	dV_n (km s^{-1})	dV_W (km s^{-1})
CH_3OH	143.86580	28.3	2.9 ± 0.8	6.7 ± 4.1	3.2 ± 0.8	7.5 ± 4.1
CH_3OH	143.16952	113	3.2 ± 0.8	6.1 ± 4.1	2.8 ± 0.8	5.8 ± 4.1
$HCOOCH_3$	143.23420	47.3	2.3 ± 0.8	5.8 ± 4.1	1.6 ± 0.8	4.1 ± 4.1
$HCOOCH_3$	143.24051	47.3	2.8 ± 0.8	5.8 ± 4.1	1.9 ± 0.8	4.1 ± 4.1
$HCOOCH_3$	163.82968	62.5	2.4 ± 0.7	6.7 ± 3.6	2.0 ± 0.7	4.7 ± 3.6
$HCOOCH_3$	163.83553	62.5	1.9 ± 0.7	3.6 ± 3.6	2.4 ± 0.7	4.4 ± 3.6
$HCOOCH_3$	163.96039	64.5	5.3 ± 0.7	6.9 ± 3.6	4.1 ± 0.7	5.9 ± 3.6
$HCOOCH_3$	163.96188	64.5	…	…	…	…
$HCOOCH_3$	163.98746	64.5	5.2 ± 0.7	6.9 ± 3.6	0.9 ± 0.7	6.0 ± 3.6
$HCOOCH_3$	163.98891	64.5	…	…	2.2 ± 0.7	…
$HCOOCH_3$	164.20598	64.9	…	5.9 ± 3.6	0.8 ± 0.7	6.6 ± 3.6
$HCOOCH_3$	164.22382	64.9	2.1 ± 0.7	6.5 ± 3.6	2.3 ± 0.7	5.2 ± 3.6

Note. dV_n and dV_W are the non-deconvolved linewidths deduced from the spectra obtained with the narrowband and WideX correlators, respectively.

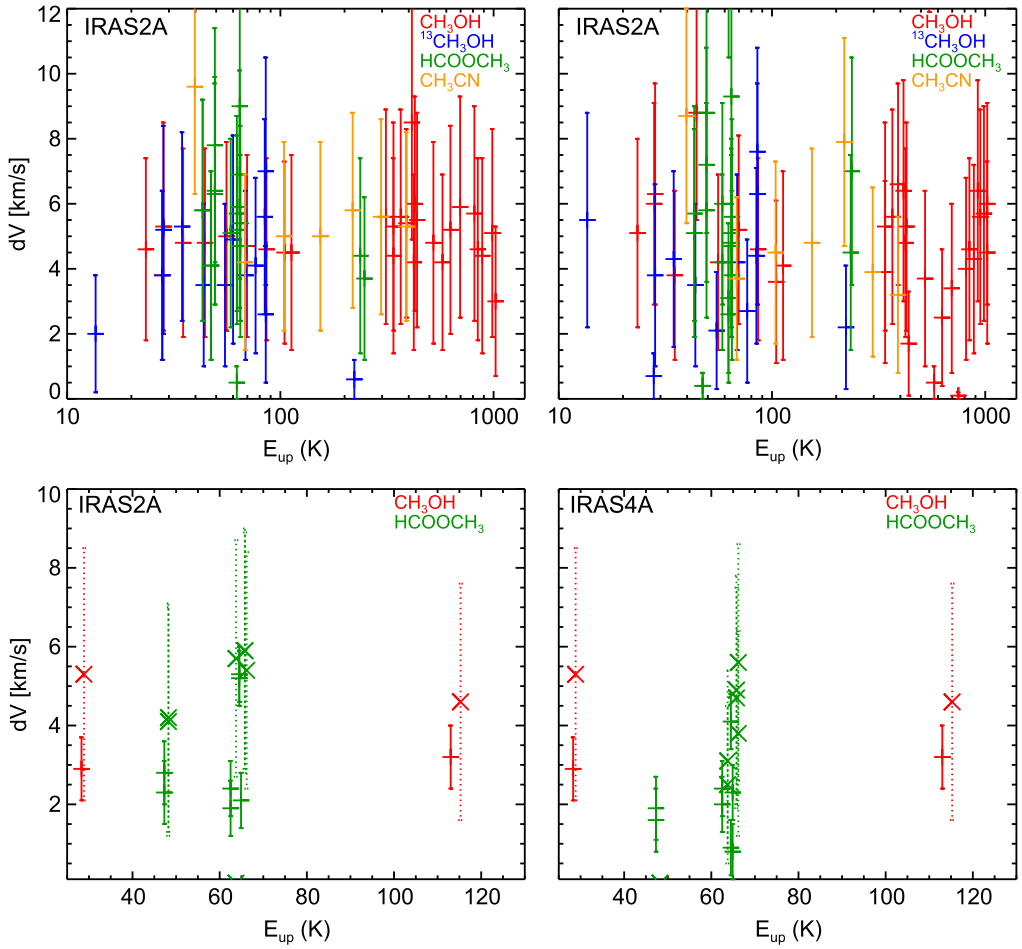

Figure 5. Top: deconvolved FWHM linewidths of CH_3OH, $^{13}CH_3OH$, $HCOOCH_3$, and CH_3CN, obtained from Gaussian fits of the WideX spectra at the source positions, as a function of E_{up}. Bottom: comparison of the FWHM linewidths deduced from the high-resolution spectra (plus signs with solid error bars) with the deconvolved FWHM linewidths from the WideX spectra (cross signs with dotted error bars) for the lines observed with the high spectral resolution correlators.

methanol toward high-mass and low-mass hot cores (Parise et al. 2006; Bisschop et al. 2007; Isokoski et al. 2013; Zapata et al. 2013), it is likely that low-energy transitions of CH_3OH are optically thick toward the center of protostellar envelopes, giving rise to an underestimation of their population in the rotational diagrams. Consequently, we excluded the

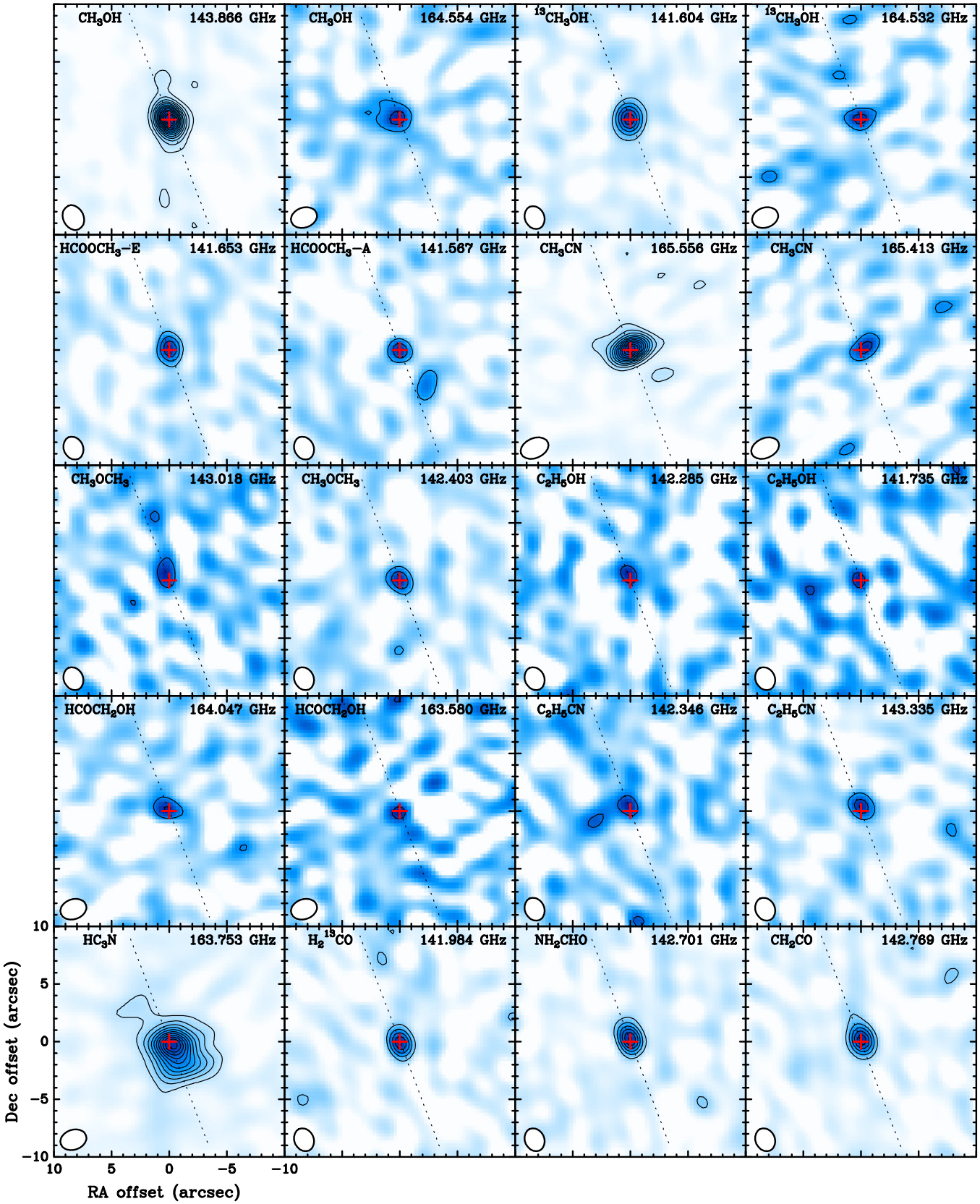

Figure 6. Integrated maps of selected lines of complex organic molecules toward IRAS 2A. For each species where several transitions have been detected, a low-excited and a high-excited transition are shown. Contour levels are in steps of 3σ. 1σ rms noise levels are the following: 38.5 and 18.2 mJy km s^{-1} for CH_3OH, 13.3 and 28.9 mJy km s^{-1} for $^{13}CH_3OH$, 13.0 and 14.6 mJy km s^{-1} for $HCOOCH_3$, 35.3 and 26.5 mJy km s^{-1} for CH_3CN, 15.5 and 9.64 mJy km s^{-1} for CH_3OCH_3, 11.6 and 14.5 mJy km s^{-1} for C_2H_5OH, 21.7 and 19.5 mJy km s^{-1} for $HCOCH_2OH$, 10.9 and 10.8 mJy km s^{-1} for C_2H_5CN, 24.8 mJy km s^{-1} for HC_3N, 13.6 mJy km s^{-1} for $H_2^{13}CO$, 17.6 mJy km s^{-1} for NH_2CHO, 12.0 mJy km s^{-1} for CH_2CO. The direction of the outflow is depicted by the dotted line.

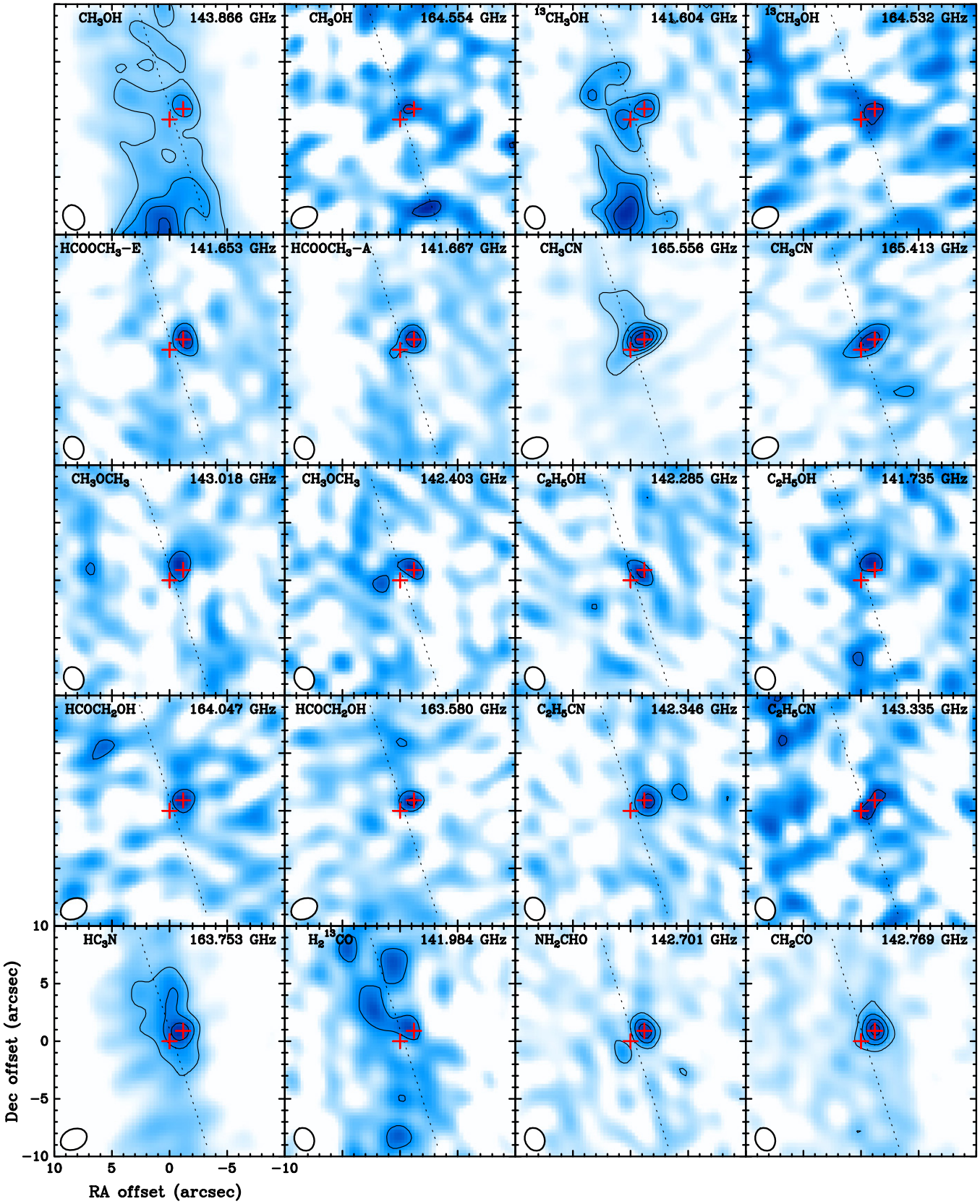

Figure 7. Integrated maps of selected lines of complex organic molecules toward IRAS 4A. For each species where several transitions have been detected, a low-excited and a high-excited transition are shown. Contour levels are in steps of 3σ. 1σ rms noise levels are the following: 81.9 and 22.8 mJy km s^{-1} for CH_3OH, 27.4 and 32.9 mJy km s^{-1} for $^{13}CH_3OH$, 25.4 and 24.5 mJy km s^{-1} for $HCOOCH_3$, 43.6 and 24.0 mJy km s^{-1} for CH_3CN, 16.9 and 11.4 mJy km s^{-1} for CH_3OCH_3, 12.4 and 19.8 mJy km s^{-1} for C_2H_5OH, 18.8 and 17.2 mJy km s^{-1} for $HCOCH_2OH$, 11.6 and 16.0 mJy km s^{-1} for C_2H_5CN, 109 mJy km s^{-1} for HC_3N, 27.8 mJy km s^{-1} for $H_2^{13}CO$, 14.3 mJy km s^{-1} for NH_2CHO, 22.4 mJy km s^{-1} for CH_2CO. The direction of the outflow is depicted by the dotted line.

Table 4
Results from the Rotational Diagram Analysis

Molecule	N_{hc} [a] (cm^{-2})	T_{rot} (K)	X^b	X^c_{meth} (%)	$N_{hc}(SD)$ [d] (cm^{-2})	$X_{meth}(SD)$ [d] (%)
			IRAS 2A			
CH_3OH [e]	$(1.2 \pm 0.4) \times 10^{18}$	179 ± 62	$(2.5 \pm 0.9) \times 10^{-7}$	...	1.4×10^{17}	...
$^{13}CH_3OH$	$(4.8 \pm 1.3) \times 10^{16}$	164 ± 43	$(9.6 \pm 2.5) \times 10^{-9}$	...	...	...
$HCOOCH_3$	$(6.4 \pm 1.9) \times 10^{16}$	200 ± 61	$(1.3 \pm 0.4) \times 10^{-8}$	1.9 ± 0.8	$< 1.2 \times 10^{17}$	< 85
CH_3CN	$(1.0 \pm 0.2) \times 10^{16}$	289 ± 63	$(2.0 \pm 0.4) \times 10^{-9}$	0.30 ± 0.10	1.5×10^{15}	1
CH_3OCH_3	$(4.1 \pm 1.6) \times 10^{16}$	154 ± 62	$(8.2 \pm 3.3) \times 10^{-9}$	1.2 ± 0.6	$< 7.2 \times 10^{16}$	< 53
C_2H_5OH	$(5.1 \pm 2.2) \times 10^{16}$	325 ± 140	$(1.0 \pm 0.4) \times 10^{-8}$	1.5 ± 0.8	...	...
$HCOCH_2OH$	7.8×10^{15}	179 [f]	1.6×10^{-9}	0.23 ± 0.06	...	...
	2.5×10^{15}	100 [f]	5.0×10^{-10}	0.074 ± 0.019	...	...
C_2H_5CN	1.2×10^{15}	179 [f]	2.4×10^{-10}	0.036 ± 0.010	$< 1.7 \times 10^{16}$	< 13
	6.9×10^{14}	100 [f]	1.4×10^{-10}	0.021 ± 0.005	...	...
HC_3N	7.0×10^{14}	179 [f]	1.4×10^{-10}	0.021 ± 0.005	...	...
	7.1×10^{14}	100 [f]	1.4×10^{-10}	0.021 ± 0.006	...	...
$H_2^{13}CO$	6.6×10^{15}	179 [f]	1.3×10^{-9}	0.20 ± 0.05	...	...
	2.1×10^{15}	100 [f]	4.3×10^{-10}	0.063 ± 0.017	...	...
NH_2CHO	1.2×10^{16}	179 [f]	2.3×10^{-9}	0.35 ± 0.09	...	...
	4.3×10^{15}	100 [f]	8.7×10^{-10}	0.13 ± 0.03	...	...
CH_2CO	7.0×10^{15}	179 [f]	1.4×10^{-9}	0.21 ± 0.05	...	...
	2.6×10^{15}	100 [f]	5.2×10^{-10}	0.077 ± 0.020	...	...
			IRAS 4A			
CH_3OH [e]	$(6.3 \pm 3.1) \times 10^{17}$	300 ± 151	$(1.7 \pm 0.9) \times 10^{-8}$	...	2.0×10^{17}	...
$^{13}CH_3OH$	$(5.1 \pm 1.5) \times 10^{16}$	197 ± 56	$(1.4 \pm 0.4) \times 10^{-9}$	...	...	...
$HCOOCH_3$	$(5.2 \pm 3.3) \times 10^{16}$	141 ± 90	$(1.4 \pm 0.9) \times 10^{-9}$	1.5 ± 1.0	1.0×10^{17}	52
CH_3CN	$(6.5 \pm 2.9) \times 10^{15}$	360 ± 162	$(1.8 \pm 0.8) \times 10^{-10}$	0.18 ± 0.10	2.6×10^{15}	1
CH_3OCH_3	$(3.1 \pm 1.0) \times 10^{16}$	86 ± 27	$(8.5 \pm 2.6) \times 10^{-10}$	0.87 ± 0.37	$< 4.5 \times 10^{16}$	< 22
C_2H_5OH	$(4.4 \pm 1.4) \times 10^{16}$	221 ± 69	$(1.2 \pm 3.7) \times 10^{-9}$	1.2 ± 0.5	...	...
$HCOCH_2OH$	$(8.9 \pm 3.4) \times 10^{15}$	124 ± 48	$(2.4 \pm 0.9) \times 10^{-10}$	0.25 ± 0.12	...	...
C_2H_5CN	2.3×10^{15}	300 [f]	6.2×10^{-11}	0.064 ± 0.018	1.9×10^{15}	< 0.92
	8.2×10^{14}	100 [f]	2.2×10^{-11}	0.023 ± 0.007	...	...
HC_3N	6.7×10^{14}	300 [f]	1.8×10^{-11}	0.019 ± 0.005	...	...
	6.8×10^{14}	100 [f]	1.8×10^{-11}	0.019 ± 0.005	...	...
$H_2^{13}CO$	5.3×10^{15}	300 [f]	1.4×10^{-10}	0.15 ± 0.04	...	...
	1.1×10^{15}	100 [f]	3.1×10^{-11}	0.032 ± 0.009	...	...
NH_2CHO	8.5×10^{15}	300 [f]	2.3×10^{-10}	0.24 ± 0.07	...	...
	2.1×10^{15}	100 [f]	5.7×10^{-11}	0.059 ± 0.017	...	...
CH_2CO	1.6×10^{16}	300 [f]	4.2×10^{-10}	0.43 ± 0.12	...	...
	4.0×10^{15}	100 [f]	1.1×10^{-10}	0.11 ± 0.03	...	...

Notes:
[a] Column densities averaged over a source size of 0.″5 (see text).
[b] The abundances relative to H_2 are obtained from $N(H_2)$ derived at 145 GHz in Table 1 assuming a homogeneous H_2 column density within the beam.
[c] The abundance ratios are relative to the $^{13}CH_3OH$ column density multiplied by 70 (see text).
[d] Column densities derived from previous single-dish observations and scaled to a source size of 0.″5. CH_3OH: Maret et al. (2005); other COMs in IRAS 2A: Bottinelli et al. (2007); other COMs in IRAS 4A: Bottinelli et al. (2004a).
[e] N_{hc} and T_{rot} have been derived from the rotation diagram neglecting the transitions with $E_{up} < 105$ K (see text).
[f] When they could not be derived from the rotation diagram, the rotational temperatures have been assumed to be equal to the temperature of evaporation of water-ice and the rotational temperature of CH_3OH.

CH_3OH transitions with $E_{up} \leqslant 200$ K from our RD analysis. The rotational temperatures and total column densities of all species derived toward the two sources are summarized in Table 4.

For most molecules, observational data can be reasonably well fitted by a straight line with some scattering, likely due to opacity or non-LTE effects. For most of species, the column densities derived toward IRAS 2A and IRAS 4A are very similar. Column densities of CH_3OH are about $(6–12) \times 10^{17}$ cm^{-2}, while the column densities of complex organics range between 6×10^{14} and 6×10^{16} cm^{-2}. The rotational temperatures derived for most COMs are generally higher than 100 K in IRAS 2A and in IRAS 4A. Although they do not necessarily reflect the kinetic temperatures, the high rotational temperatures found in the inner protostellar envelope are in good agreement with the kinetic temperatures

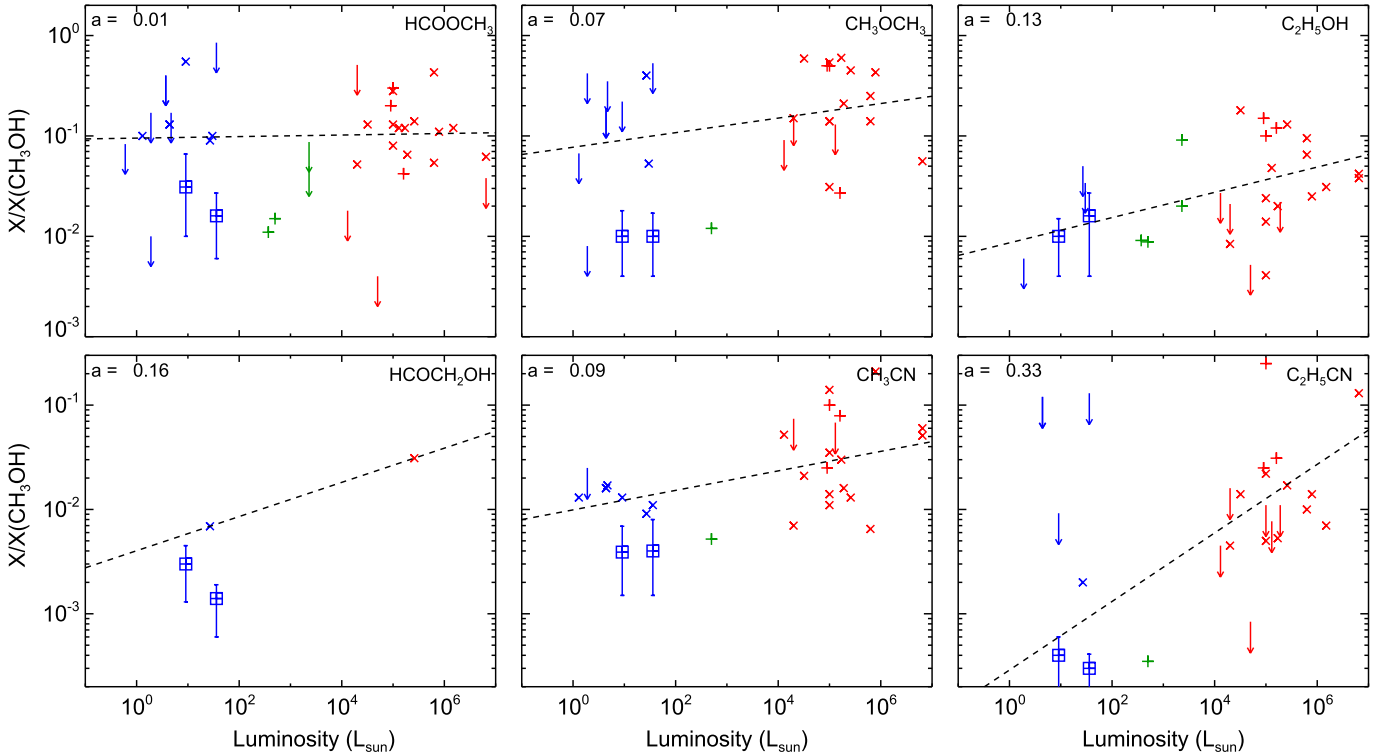

Figure 8. Abundances of COMs detected in several transitions with respect to CH_3OH toward a sample of low-mass ($L < 100\,L_\odot$; blue), intermediate-mass ($100\,L_\odot < L < 10^4\,L_\odot$; green), and high-mass ($L > 10^4\,L_\odot$; red) hot cores as a function of the protostar luminosity. Cross and plus symbols represent abundance ratios derived with single-dish telescopes and interferometers, respectively. The abundance ratios derived in this work with the Population Diagram analyses are denoted by squares with error bars. The sample of hot cores is listed in Table A10 along with their physical and chemical properties.

expected in hot corinos ($T > 100$ K). The CH_3CN population distribution can be used to estimate the kinetic temperature of the warm inner envelope because the CH_3CN population distribution over the different K ladders observed for $J = 9$ can only be modified by collisions as radiative transitions are prohibited (see Wang et al. 2010 for a more detailed discussion of the CH_3CN population in hot cores). If the energy states are thermalized and the transitions are optically thin, the kinetic temperatures within the hot corinos of IRAS 2A and IRAS 4A would be close to 290 and 360 K, respectively. As we will see in the next section, the temperatures are probably overestimated since the CH_3CN transitions are likely optically thick.

We derived a $^{12}C/^{13}C$ abundance ratio of CH_3OH of 26 and 12 in IRAS 2A and IRAS 4A, respectively. The two values are lower than the $^{12}C/^{13}C$ abundance ratio of ~70 expected in the local ISM (Boogert et al. 2002; Milam et al. 2005; Wirström et al. 2011) by a factor 2.7 and 5.8, respectively. We verified that using the same rotational temperature for CH_3OH and $^{13}CH_3OH$ only modifies the $^{12}C/^{13}C$ abundance ratios by a few percent at most. The low $^{12}C/^{13}C$ abundance ratio might be due to the different ranges of excitation of the observed transitions used to derive the column densities. We used excited transitions (with $E_{up} > 200$ K) to derive $N(^{12}CH_3OH)$, whereas only weakly excited $^{13}CH_3OH$ transitions (with $E_{up} < 225$ K) have been detected. The low ratio measured in the two protostars suggests that excited transitions of CH_3OH ($E_{up} > 200$ K) are also optically thick. An overestimation of the $^{13}CH_3OH$ column density by the RD best fit, due to the large uncertainty on the fluxes, is also possible. An analysis taking the opacities into account is therefore required to clarify this issue.

Table 5
Results of the PD Analysis of the Methanol Emission

Source	IRAS 2A	IRAS 4A
χ^2_{red}	1.4	2.1
$N(CH_3OH)$ (cm^{-2})	$5.0^{+2.9}_{-1.8} \times 10^{18}$	$1.6^{+0.6}_{-0.8} \times 10^{19}$
$N(^{13}CH_3OH)$ (cm^{-2})	$7.1^{+4.2}_{-2.6} \times 10^{16}$	$2.3^{+1.3}_{-1.1} \times 10^{17}$
θ_s ($''$)	$0.36^{+0.04}_{-0.04}$	$0.20^{+0.08}_{-0.04}$
T_{rot} (K)	140^{+20}_{-20}	140^{+30}_{-30}

4.2. Population Diagrams (PDs)

We used the so-called PD analysis following the method described by Goldsmith & Langer (1999) to investigate the effect of optical depth on the column densities of each level. We applied the PD analysis where four or more transitions were detected for each species. Briefly, the PD analysis includes the influence of optical depths on the level populations assumed to be at LTE, following the formula

$$\ln\left(\frac{N_{up}}{g_{up}}\right) = \ln\left(\frac{N_{tot}}{Q_{rot}}\right) - \frac{E_{up}}{kT_{rot}} - \ln\left(\frac{\Omega_a}{\Omega_s}\right) - \ln\left(C_\tau\right), \quad (3)$$

Table 6
Results from the Population Diagram Analysis for the COM Emission

Molecule	N_{hc} (cm^{-2})	T_{rot} (K)	Source Size ($''$)	X^a	X^b_{meth}
			IRAS 2A		
CH_3OH	$5.0^{+2.9}_{-1.8} \times 10^{18}$	140^{+20}_{-20}	$0.36^{+0.04}_{-0.04}$	$1.0^{+0.6}_{-0.4} \times 10^{-6}$	...
$^{13}CH_3OH$	$7.1^{+4.2}_{-2.6} \times 10^{16}$	140^{+20}_{-20}	$0.36^{+0.04}_{-0.04}$	$1.4^{+0.8}_{-0.5} \times 10^{-8}$	...
$HCOOCH_3$	$7.9^{+4.6}_{-1.6} \times 10^{16}$	160^{+50}_{-30}	0.36[c]	$1.6^{+0.9}_{-0.3} \times 10^{-8}$	$1.6^{+1.1}_{-1.0}$
CH_3CN	$2.0^{+1.2}_{-0.4} \times 10^{16}$	130^{+230}_{-40}	0.36[c]	$4.0^{+2.4}_{-0.8} \times 10^{-9}$	$0.40^{+0.28}_{-0.25}$
CH_3OCH_3	$5.0^{+2.9}_{-1.0} \times 10^{16}$	110^{+60}_{-20}	0.36[c]	$1.0^{+0.6}_{-0.2} \times 10^{-8}$	$1.0^{+0.7}_{-0.6}$
C_2H_5OH	$7.9^{+4.6}_{-4.0} \times 10^{16}$	270^{+230}_{-80}	0.36[c]	$1.6^{+0.9}_{-0.8} \times 10^{-8}$	$1.6^{+1.1}_{-1.2}$
$HCOCH_2OH$	6.8×10^{15}	140[d]	0.36[d]	1.4×10^{-9}	$0.14^{+0.05}_{-0.08}$
C_2H_5CN	1.5×10^{15}	140[d]	0.36[d]	3.0×10^{-10}	$0.030^{+0.011}_{-0.017}$
HC_3N	9.3×10^{14}	140[d]	0.36[d]	1.9×10^{-10}	$0.019^{+0.007}_{-0.011}$
$H_2{}^{13}CO$	6.3×10^{15}	140[d]	0.36[d]	1.3×10^{-9}	$0.13^{+0.05}_{0.07}$
NH_2CHO	1.2×10^{16}	140[d]	0.36[d]	2.4×10^{-9}	$0.24^{+0.09}_{-0.14}$
CH_2CO	6.8×10^{15}	140[d]	0.36[d]	1.4×10^{-9}	$0.14^{+0.05}_{-0.08}$
			IRAS 4A		
CH_3OH	$1.6^{+0.6}_{-0.8} \times 10^{19}$	140^{+30}_{-30}	$0.20^{+0.08}_{-0.04}$	$4.3^{+2.5}_{-2.1} \times 10^{-7}$	...
$^{13}CH_3OH$	$2.3^{+1.3}_{-1.1} \times 10^{17}$	140^{+30}_{-30}	$0.20^{+0.08}_{-0.04}$	$6.2^{+3.5}_{-3.0} \times 10^{-9}$	...
$HCOOCH_3$	$5.0^{+5.0}_{-1.8} \times 10^{17}$	60^{+20}_{-10}	0.20[c]	$1.4^{+1.4}_{-0.5} \times 10^{-8}$	$3.1^{+3.5}_{-2.1}$
CH_3CN	$6.3^{+3.6}_{-1.3} \times 10^{16}$	200^{+110}_{-40}	0.20[c]	$1.7^{+1.0}_{-0.4} \times 10^{-9}$	$0.39^{+0.30}_{-0.24}$
CH_3OCH_3	$1.6^{+0.9}_{-0.3} \times 10^{17}$	80^{+40}_{-20}	0.20[c]	$4.3^{+2.5}_{-0.9} \times 10^{-9}$	$1.0^{+0.8}_{-0.6}$
C_2H_5OH	1.6×10^{17}	140[d]	0.20[d]	4.3×10^{-9}	$1.0^{+0.5}_{-0.6}$
$HCOCH_2OH$	4.8×10^{16}	140[d]	0.20[d]	1.3×10^{-9}	$0.30^{+0.15}_{-0.17}$
C_2H_5CN	6.4×10^{15}	140[d]	0.20[d]	1.7×10^{-10}	$0.040^{+0.020}_{-0.023}$
HC_3N	2.9×10^{15}	140[d]	0.20[d]	7.8×10^{-11}	$0.018^{+0.009}_{-0.010}$
$H_2{}^{13}CO$	1.1×10^{16}	140[d]	0.20[d]	3.0×10^{-10}	$0.069^{+0.034}_{0.040}$
NH_2CHO	1.9×10^{16}	140[d]	0.20[d]	5.1×10^{-10}	$0.12^{+0.06}_{-0.07}$
CH_2CO	3.4×10^{16}	140[d]	0.20[d]	9.2×10^{-10}	$0.21^{+0.10}_{-0.12}$

Notes:
[a] The abundances relative to H_2 are obtained from $N(H_2)$ derived at 145 GHz in Table 1 assuming a homogeneous H_2 column density within the beam.
[b] The abundances relative to CH_3OH were computed from $N(CH_3OH)$ derived from the PD analysis of the CH_3OH and $^{13}CH_3OH$ emissions and adapted for the same source size.
[c] The source size was assumed to be equal to that of methanol when the size could not be constrained.
[d] The source size and rotational temperatures were assumed to be equal to those of methanol.

where N_{tot} is the total column density of the species in question, N_{up} is the observed column density of the upper state of the species with an upper energy E_{up} including the opacity effect, Q_{rot} is the partition function, Ω_a is the beam solid angle, and Ω_s is the source solid angle. C_τ is given by

$$C_\tau = \frac{\tau}{1 - \exp(-\tau)}, \quad (4)$$

with τ being the optical depth. τ can be expressed as

$$\tau = \frac{c^3}{8\pi\nu_0^3}\frac{A_{ul}}{\Delta V}\frac{g_{up}N_{tot}}{Q_{rot}}\exp\left(\frac{-E_{up}}{kT_{rot}}\right)\left(\exp\left(\frac{h\nu_0}{kT_{rot}}\right) - 1\right), \quad (5)$$

where c is the speed of light, A_{ul} is the Einstein-A coefficient of spontaneous emission, and ΔV is the FWHM fixed to 3 km s^{-1}. We performed a reduced χ^2_{red} minimization by running a grid of 125,000 models covering a large parameter space in rotational temperature T_{rot} (50 values between 10 and 500 K), total column density in the source N_{tot} (50 values between 10^{15} and 10^{20} cm^{-2}), and source size θ_s (50 values between $0''.04$ and $2''$). At LTE, the column density of every upper state N_{up} can be derived for each set of N_{tot}, T_{rot}, and source solid angle $\Omega_s = \theta_s^2$ according to Equation (3). The best-fit model populations are plotted together with the observed populations of the levels in Figures A1 and A2 and are marked by red cross symbols. Tables 5 and 6 summarize the parameters of the best-fit models.

We started the PD analysis by simultaneously modeling the population distribution of $^{12}CH_3OH$ and $^{13}CH_3OH$. For this purpose, we assumed a $^{12}C/^{13}C$ abundance ratio of 70 following Boogert et al. (2002) and the same rotational temperature for the two isotopologues. The population modeling of high-energy $^{12}CH_3OH$ ($400 < E_{up} < 1100$ K) and low-energy $^{13}CH_3OH$ optically thin transitions allowed us to constrain the rotational temperature through the determination of the slope of the level populations, leaving only a degeneracy between N_{tot} and θ_s. Since the optical depth τ of each level depends on the total column density N_{tot}, low-energy optically thick transitions from $^{12}CH_3OH$ can be used to constrain N_{tot} and θ_s.

Table 5 presents the results of the PD analysis of the methanol population distribution. The methanol emission is relatively well modeled by the PD model for the two sources. The PD analysis converges toward one single set of input physical parameters ($N_{\rm tot}$, θ_s, $T_{\rm rot}$) with $\chi^2_{\rm red}$ of about 1.5–2 and with uncertainties up to 50% at a 1σ level for the column densities. The PD model was able to reproduce the population of most transitions within their uncertainties except the population of some low-energy transitions of $^{13}CH_3OH$ in IRAS 2A and of $^{12}CH_3OH$ in IRAS 4A, which tend to be underestimated. The rotational temperatures of methanol deduced from the PD analysis are similar in IRAS 2A and IRAS 4A (∼140 K). However, the source size derived for IRAS 2A is larger than for IRAS 4A (∼0.″36 versus ∼0.″20). The source size deduced for IRAS 2A is in good agreement with the size estimated by Maret et al. (2004), but we found a smaller source size for IRAS 4A, by a factor of 2.5. The source size of IRAS 2A of 0.″36, corresponding to a radius of 42 AU at 235 pc, is also consistent with the FWHM emission size of the CH_3OH transitions deduced by Maury et al. (2014) from elliptical Gaussian fits that range between 25 and 70 AU.

For all other COMs, the low number of observed transitions and the relatively high uncertainty on the derived column density of each level generate a degeneracy between the input parameters and prevent the PD model from converging toward one single set of input parameters: the observations are overfitted and can be reproduced by a large range of parameters giving χ^2 lower than 1. Therefore, we decided to fix the source size for the COM emission to the size of the methanol emission, assuming that all COMs will evaporate with methanol in spite of their slightly different binding energies. Even by fixing the source size, the analysis of the glycolaldehyde and ethyl cyanide populations toward the two sources and of the ethanol population toward IRAS 4A did not allow us to converge toward one set of $N_{\rm tot}$ and $T_{\rm rot}$. For other molecules, we were able to deduce a unique column density with relatively small uncertainties. As seen in Figures A1 and A2, the observed population distribution is well reproduced by the best-fit model since most of the column densities of upper energy levels predicted by the best-fit model lie within the range of uncertainties of the observed data. The best-fit models of the PDs generally consist of lower rotational temperatures and higher total column densities than the values derived with the RDs in order to reproduce the population of the optically thick transitions. For instance, the spread of the population distribution of the low upper energy levels ($E_{\rm up} \leqslant 120$ K) of CH_3OH, $^{13}CH_3OH$, $HCOOCH_3$, or CH_3CN are explained by opacity effects. For these species, transitions showing a decrease of their population are optically thick with τ higher than 1.

For species where the PD analysis was not able to converge toward one set of input parameters (namely, glycolaldehyde, ethanol, and ethyl cyanide) and for molecules showing only one detected transition, we fixed the source size and the rotational temperature to the values found for methanol. Results of this analysis are shown in Table 6.

Most transitions of COMs whose collision rates have been computed (CH_3OH, CH_3CN, and HC_3N) have critical densities that range between 10^5 and 10^7 cm^{-3} at 100 K. They are therefore likely lower than the densities found in the hot corinos of IRAS 2A and IRAS 4A ($n_{\rm H2} > 1.3 \times 10^8$ cm^{-3} following the density profiles of the two envelopes derived by Maret et al. 2004). Given the good fit to the observational data with our LTE PD analysis, it is likely that the observed species are at LTE. Most of the scattering of the population distribution can therefore be attributed to opacity effects only.

5. DISCUSSION

5.1. Abundances in IRAS 2A and IRAS 4A

Methanol is likely the most abundant complex organics and is believed to be the precursor molecule of several COMs. It is therefore worth comparing the abundance of COMs with respect to methanol to quantify the efficiency of their formation. Moreover, column densities of COMs and methanol have been derived with similar methods and from the same observational data. The estimates of the abundance ratios are therefore more accurate than the absolute abundances derived with respect to H_2 that are likely underestimated due to an overestimate of the H column density, which may include both warm and any cold gas in a shielded disk-like region (see Persson et al. 2012). Tables 4 and 6 list the abundance ratios of the COMs with respect to methanol for the RD and PD analyses. The two targeted sources seem to have a similar chemical composition since the COM abundance ratios differ by only a factor of two at maximum. Methyl formate is the most abundant COM of our sample, with an abundance of 1.5%–3%, followed by ethanol (1%–1.5%) and di-methyl ether (1%). Other COMs are detected with abundances lower than 1%: glycolaldehyde and methyl cyanide show abundances of 0.15% and 0.40%, respectively, while ethyl cyanide is detected with an abundance of 0.03%–0.04%.

Table 4 compares the column densities and abundance ratios deduced from the RD analysis with previous single-dish studies by Bottinelli et al. (2004a), Maret et al. (2005), Bottinelli et al. (2007) carried out toward IRAS 2A and IRAS 4A. The column densities obtained from these previous observations suffer from several limitations: most detected transitions have low upper energy levels, and the large beam of single-dish telescopes encompasses the cold envelope where weakly excited lines may have contaminated the hot corino emission (see the interferometric maps in Figures 6 and 7). Consequently, the rotational temperatures and column densities derived with the PdBi are higher ($T_{\rm rot}$ = 80–290 and 300–360 K in this work toward IRAS 2A and IRAS 4A versus 100 and 25 K, respectively, and higher column densities up to one order of magnitude), since the interferometric observations probe material closer to the central protostars. The abundance ratios deduced from previous single-dish studies have also higher relative uncertainties than in this work due to the different telescope calibrations since the observations of methanol and COMs have been carried out separately. The abundances relative to methanol derived from our interferometric observations therefore differ from the abundances obtained with the single-dish observations, the latter being usually overestimated. The methyl formate abundance derived in IRAS 2A of 2% is consistent with the upper limit of 85% by Bottinelli et al. (2007). However, the abundance derived in IRAS 4A of ∼3% is 18 times lower than the value derived by Bottinelli et al. (2004a) and using the

Table 7
Averaged COM Abundances (in %) with Respect to Methanol

Molecule	LMP	IMP	HMP	G13	R01
$HCOOCH_3$	14^{+41}_{-7}	1.3 ± 0.2	14^{+18}_{-6}	0.082–0.84	0.013–0.67
CH_3OCH_3	12^{+28}_{-10}	1.2	30^{+23}_{-18}	0.44–0.74	0.62–18
$HCOCH_2OH$	$0.38^{+0.31}_{-0.18}$	/	3.1	0.54–1.3	···
C_2H_5OH	$1.3^{+0.3}_{-0.3}$	$3.2^{+5.9}_{-2.0}$	$6.4^{+6.6}_{-4.1}$	0.50–2.6	15–23
CH_3CN	$1.1^{+0.4}_{-0.5}$	0.52	$5.1^{+7.8}_{-3.3}$	0.034–0.45	3.0–3.7
C_2H_5CN	$0.090^{+0.11}_{-0.055}$	/	$4.1^{+16}_{-2.8}$	0.052–0.79	···

Note. LMP, IMP, and HMP stand for low-mass ($L < 100\,L_\odot$), intermediate-mass ($100\,L_\odot < L < 10^4\,L_\odot$), and high-mass ($10^4\,L_\odot < L$) protostars. The two abundances in the column "G13" are the peak abundances of the "Fast" and "Slow" models of Garrod (2013). The two abundances in the column "R01" are the peak abundances of the models including ammonia at $T = 100$ and $T = 300$ K of Rodgers & Charnley (2001).

column density of CH_3OH derived by Maret et al. (2005). The higher abundance of methyl formate with respect to methanol in IRAS 4A derived from single-dish observations is explained by the lower column density of methanol derived in Maret et al. (2005) assuming optically thin emission. For the same reasons, the abundances of methyl cyanide derived in the two sources by our PD analysis are also lower, by a factor of 3–6, than the abundances obtained by Bottinelli et al. (2007). Di-methyl ether, ethanol, and ethyl cyanide have not been detected with single-dish telescopes toward IRAS 2A and IRAS 4A, but their upper limits agree well with our observations.

We report here the first detection of glycolaldehyde in low-mass protostars other than IRAS 16293. Glycolaldehyde co-exists with its isomer methyl formate with a $[HCOOCH_3]/[HCOCH_2OH]$ abundance ratio of 12^{+7}_{-2} toward IRAS 2A and of 10^{+10}_{-4} toward IRAS 4A. These abundance ratios are similar to the ratios of ∼13 found in the sources A and B of the IRAS 16293 protostellar binary system by Jørgensen et al. (2012) from high angular resolution ALMA observations. They are also consistent with the ratios derived toward SgrB2(N) ranging from 52 in the hot core (Hollis et al. 2001) to 5 found on more extended scales (Hollis et al. 2000).

5.2. Comparison with Other Sources

The COM abundances derived in this work are compared with other published data of low-mass, intermediate-mass, and high-mass hot cores obtained with single-dish and interferometric sub-mm telescopes in Figure 8 showing the COM abundances as a function of the protostar luminosity. Table A10 lists the abundances of selected COMs toward the hot cores shown in Figure 8 along with the references. For this purpose, we only selected observational studies where several transitions of methanol were detected. For most of the works, COMs and methanol were detected simultaneously and the abundance ratios were derived from the main isotopologue CH_3OH, either by assuming optically thin emission and LTE population (MacDonald et al. 1996; Ikeda et al. 2001; Beuther et al. 2007, 2009; Öberg et al. 2011, 2014; Palau et al. 2011), by neglecting optically thick lines in the RD analysis (Bisschop et al. 2007; Isokoski et al. 2013), or by taking the opacity of the lines into account in their model (Nummelin et al. 2000; Qin et al. 2010; Crockett et al. 2014; Neill et al. 2014). Fuente et al. (2014) derived the methanol abundances from the $^{13}CH_3OH$ isotopologue. For IRAS 16293, we combined the CH_3OH absolute abundance derived by Schöier et al. (2002) with the COM abundances obtained by Jaber et al. (2014), both from a radiative transfer modeling, to obtain the abundance ratios. We also derived the glycolaldehyde abundance from Jørgensen et al. (2012).

Overall, the abundance ratios of COMs estimated toward IRAS 2A and IRAS 4A in this work tend to be lower than the abundances derived in other low-mass protostars from single-dish observations. For example, methyl formate and methyl cyanide have been detected toward five other low-mass sources and show abundances of 5%–50% and 0.8%–1.7% respectively, representing a factor of 1.5–15 and 1.5–3 higher than in our work. Since these observations suffer from the same limitations as the single-dish observations by Bottinelli et al. (2004a, 2007) presented in the previous section (low number of detected transitions, low upper energy levels of detected transitions, large beam encompassing the external envelope), the discrepancy likely comes from the differences in the observational methods and does not necessarily reflect differences in the chemistry between the sources.

Table 7 summarizes the mean abundance ratios of COMs in low-mass, intermediate-mass, and high-mass protostars. Along with Figure 8, they allow us to investigate any possible correlation of the COM abundances with the protostar luminosity. For each molecule, the data have been fitted by a linear curve depicted by the dashed curve whose slope a is shown at the top left of each panel of Figure 8, by considering detected ratios only. It can be noticed that the abundances of the six COMs tend to slightly increase with the protostar luminosity. However, for all species but C_2H_5CN, the increase remains negligible compared to the dispersion of the abundance ratio values. We can conclude that the abundance ratio of these COMs stays relatively constant with the protostar luminosity within six orders of magnitude. In spite of their lower luminosities, inducing lower temperatures, and smaller sizes, low-mass protostars seem to be as chemically complex as high-mass protostars.

5.3. Comparison with Chemical Model Predictions

We compare the observed abundance ratios in low-mass, intermediate-mass, and high-mass protostars with the results of two astrochemical models in Table 7. The model of Garrod (2013) is a multilayer gas-grain astrochemical model in which COMs are assumed to be mostly formed at the

surface of interstellar ices during the warm-up protostellar phase ($30\,K < T < 100$ K) through radical recombination induced by the UV photodissociation of the main ice components. In the model of Rodgers & Charnley (2001), COMs are only formed by warm gas phase chemistry for a set of constant physical parameters representative of hot cores ($n_H = 10^7$ cm^{-3}; $T = 100$ and 300 K) after the sublimation of interstellar ices with typical ice composition, already containing C_2H_5OH with an abundance of 20% with respect to CH_3OH. Although the rates of some key reactions for the formation of COMs have been lowered meanwhile, such as the methyl cation transfer reaction between H_2CO and $CH_3OH_2^+$ or the electronic recombination of protonated COMs ions, this model still provides a good basis to estimate the formation efficiency of methyl formate, di-methyl ether, and methyl cyanide in the gas phase.

Both models tend to underpredict the abundance of methyl formate relative to methanol observed in low-mass and high-mass protostars by at least 1–2 orders of magnitude. Moreover, the model of Garrod (2013) also underpredicts the $[HCOOCH_3]/[HCOCH_2OH]$ abundance ratio by two orders of magnitude since it seems to reproduce well the observed abundance of glycolaldehyde. This comparison suggests that the chemical network forming methyl formate either in the gas phase or on ices is still incomplete. Possible alternative branching ratios for the photodissociation of CH_3OH on ices or other gas phase reactions involving HCOOH could enhance its formation. The observed abundances of di-methyl ether and methyl cyanide with respect to methanol can be reproduced by the gas phase model of Rodgers & Charnley (2001) only. The absolute abundances of these two molecules are similar in the two models (10^{-8} to 10^{-7} for di-methyl ether and 10^{-9} to 10^{-8} for methyl cyanide), showing that warm gas phase chemistry tends to be as efficient as surface chemistry to produce these COMs. However, the difference in the abundances comes from the efficient destruction of methanol in the warm gas in the model of Rodgers & Charnley (2001) increasing the abundance ratio of COMs. No efficient formation routes in the gas phase have been proposed for glycolaldehyde and ethanol, but their formation at the surface of interstellar ices seems to be efficient enough to reproduce the observations toward low-mass and high-mass protostars. The abundance of ethyl cyanide shows an increase of almost two orders of magnitude between low-mass and high-mass protostars. Grain surface chemistry is able to reproduce the observations toward low-mass protostars but not toward high-mass hot cores. It is also possible that models also missed gas phase reactions, as it was the case for methyl formate, where a new gas phase reaction has been recently recognized by Balucani et al. (2015).

6. CONCLUSIONS

In this work, we have presented interferometric multi-line observations of methanol (CH_3OH, $^{13}CH_3OH$) and various COMs toward the two bright low-mass protostars NGC 1333-IRAS 2A and -IRAS 4A, carried out with the PdBi at an angular resolution of $\sim 2''$. We summarize here the main conclusions of this work:

1. Except for methanol, none of the transitions from complex organics are spatially resolved with the interferometer, confirming that most of the emission comes from the inner arcsecond from the central protostars.
2. Low-energy transitions ($E_{up} \leqslant 120$ K) of methanol show extended emission around IRAS 4A and trace the outflows driven by the central protostar.
3. We detected a high number of transitions (up to 45 for methanol) from COMs with a wide range of upper energy levels (up to 1000 K for methanol) allowing us to accurately derive their column densities with the use of LTE methods.
4. The abundances derived in this work, of a few percent for methyl formate and di-methyl ether and of $\sim$0.5% for methyl cyanide, for instance, seem to be slightly lower than the abundances found toward other low-mass protostars. However, the difference likely comes from differences in the observational methods rather than different chemistries taking place in these protostars.
5. We report the first detection of glycolaldehyde in low-mass protostars other than IRAS 16293, with a methyl formate-to-glycol aldehyde abundance ratio of 12 and 10 in IRAS 2A and IRAS 4A, respectively.
6. The analysis of the variation of the COM abundance ratios with the protostellar luminosity shows that low-mass hot corinos seem to be as chemically rich as high-mass hot cores, in spite of their lower temperatures and their smaller sizes.
7. Comparison with theoretical models shows that the two theories of COM formation, either in the gas phase or at the surface of interstellar ices, tend to underpredict the formation of methyl formate by one to orders of magnitude. The comparison of the abundance ratios of other molecules favors a gas phase formation for di-methyl ether and methyl cyanide and a formation on ices for ethanol, ethyl cyanide, and glycolaldehyde.

The authors are grateful to the anonymous referee whose comments contributed to improving the quality of the present paper. This work was supported by NASA's Origins of Solar Systems and Exobiology Programs. V.T. acknowledges support from the NASA postdoctoral program. A.L.-S. and C.C. acknowledge financing from the French space agency CNES.

APPENDIX

Tables A1 to A9 present the parameters of transitions from complex organics detected toward IRAS 2A and/or IRAS 4A. Figures A1 and A2 compare the observed and model population diagrams of complex organics with more than four detected transitions toward IRAS 2A and/or IRAS 4A. Table A10 lists the column densities and abundance ratios with respect to methanol for a selection of complex organics toward high-mass, intermediate-mass, and low-mass protostars observed in previous works.

Table A1
Line Parameters of CH_3OH Lines Observed toward IRAS 2A and IRAS 4A-NW

					IRAS 2A				IRAS 4A			
N	Frequency (GHz)	Transition	E_{up} (K)	A_{ul} (s^{-1})	Beam Size ($''\times''$, ^{o})	Source Size[a] ($''\times''$, ^{o})	Flux[b] (Jy km s^{-1})	dV_W[c] (km s^{-1})	Beam Size ($''\times''$, ^{o})	Source Size (PA)[a] ($''\times''$, ^{o})	Flux[b] (Jy km s^{-1})	dV_W [c] (km s^{-1})
1	145.093754	3_0-2_0 E1, $v_t = 0$	27.1	1.23(−5)	2.08 × 1.65 (30)	1.65 × 1.04 (19)	2.62 ± 0.53	⋯	2.16 × 1.73 (25)	outflow	2.54 ± 0.51	⋯
	145.097435	3_0-2_0 E2, $v_t = 0$	19.5	1.10(−5)	⋯	⋯	⋯	⋯	⋯	⋯	⋯	⋯
	145.103185	3_0-2_0 A^+, $v_t = 0$	13.9	1.23(−5)	⋯	⋯	⋯	⋯	⋯	⋯	⋯	⋯
2	165.050175	1_1-1_0 E1, $v_t = 0$	23.4	2.35(−5)	2.31 × 1.72 (110)	1.01 × 0.87 (11)	1.28 ± 0.26	5.8	2.39 × 1.77 (114)	outflow	0.38 ± 0.08	6.2
3	165.061130	2_1-2_0 E1, $v_t = 0$	28.0	2.34(−5)	2.31 × 1.72 (110)	1.18 × 0.83 (50)	1.49 ± 0.30	5.2	2.39 × 1.77 (114)	outflow	0.56 ± 0.12	7.0
4	143.865795	3_1-2_1 A^+, $v_t = 0$	28.3	1.07(−5)	2.24 × 1.77 (25)	0.83 × 0.63 (10)	1.02 ± 0.21	6.7	2.24 × 1.77 (25)	outflow	0.44 ± 0.13	7.5
5	165.099240	3_1-3_0 E1, $v_t = 0$	35.0	2.33(−5)	2.31 × 1.72 (110)	1.19 × 1.07 (30)	1.44 ± 0.29	6.0	2.39 × 1.77 (114)	outflow	0.39 ± 0.08	5.2
6	145.124332	3_0-2_0 A^-, $v_t = 0$	51.6	6.89(−6)	2.08 × 1.65 (30)	1.05 × 0.71 (32)	3.18 ± 0.64	⋯	2.16 × 1.73 (25)	outflow	1.65 ± 0.33	⋯
	145.126191	3_2-2_2 E1, $v_t = 0$	36.2	6.77(−6)	⋯	⋯	⋯	⋯	⋯	⋯	⋯	⋯
	145.126386	3_2-2_2 E2, $v_t = 0$	39.8	6.86(−6)	⋯	⋯	⋯	⋯	⋯	⋯	⋯	⋯
	145.131864	3_1-2_1 E1, $v_t = 0$	35.0	1.12(−5)	⋯	⋯	⋯	⋯	⋯	⋯	⋯	⋯
	145.133415	3_2-2_2 A^+, $v_t = 0$	51.6	6.89(−6)	⋯	⋯	⋯	⋯	⋯	⋯	⋯	⋯
7	165.190475	4_1-4_0 E1, $v_t = 0$	44.3	2.32(−5)	2.31 × 1.72 (110)	1.26 × 1.02 (76)	1.96 ± 0.40	6.0	2.39 × 1.77 (114)	outflow	0.64 ± 0.13	9.5
8	165.369341	5_1-5_0 E1, $v_t = 0$	55.9	2.31(−5)	2.54 × 1.71 (113)	1.10 × 0.92 (42)	1.59 ± 0.32	6.1	2.38 × 1.76 (114)	outflow	0.68 ± 0.14	5.5
9	165.678649	6_1-6_0 E1, $v_t = 0$	69.8	2.30(−5)	2.54 × 1.71 (113)	1.08 × 0.99 (54)	1.52 ± 0.31	5.9	2.38 × 1.76 (114)	outflow	0.55 ± 0.11	6.3
10	166.169098	7_1-7_0 E1, $v_t = 0$	86.1	2.28(−5)	2.54 × 1.71 (113)	1.06 × 0.99 (30)	1.46 ± 0.29	5.8	2.38 × 1.76 (114)	outflow	0.54 ± 0.11	5.8
11	166.898566	8_1-8_0 E1, $v_t = 0$	104.6	2.28(−5)	2.54 × 1.71 (113)	1.02 × 0.56 (44)	1.45 ± 0.29	5.7	2.38 × 1.76 (114)	outflow	0.51 ± 0.11	5.0
12	143.169517	7_3-8_2 E1, $v_t = 0$	112.7	4.13(−6)	2.31 × 1.82 (26)	point	0.63 ± 0.22	6.1	2.31 × 1.82 (26)	outflow	0.24 ± 0.08	5.8
13	144.728359	3_2-2_2 A^+, $v_t = 1$	312.6	6.78(−6)	2.08 × 1.65 (30)	0.68 × 0.64 (−73)	0.80 ± 0.16	6.9	2.16 × 1.73 (25)	point	0.23 ± 0.05	⋯
	144.728782	3_2-2_2 E2, $v_t = 1$	378.5	6.83(−6)	⋯	⋯	⋯	⋯	⋯	⋯	⋯	⋯
	144.729074	3_2-2_2 A^-, $v_t = 1$	312.6	6.78(−6)	⋯	⋯	⋯	⋯	⋯	⋯	⋯	⋯
14	144.733262	3_2-2_2 E1, $v_t = 1$	413.8	6.80(−6)	2.08 × 1.65 (30)	0.38	0.96 ± 0.19	9.4	2.16 × 1.73 (25)	0.48	0.42 ± 0.09	7.6
	144.734429	3_1-2_1 E1, $v_t = 1$	305.4	1.09(−5)	⋯	⋯	⋯	⋯	⋯	⋯	⋯	⋯
	144.736349	3_0-2_0 E1, $v_t = 1$	314.5	1.22(−5)	⋯	⋯	⋯	⋯	⋯	⋯	⋯	⋯
15	144.589854	3_1-2_1 A^+, $v_t = 1$	339.1	1.09(−5)	2.08 × 1.65 (30)	0.59	0.37 ± 0.08	6.0	2.16 × 1.73 (25)	0.3	0.21 ± 0.06	6.7
16	144.878576	3_1-2_1 A^-, $v_t = 1$	339.2	1.09(−5)	2.08 × 1.65 (30)	0.35	0.43 ± 0.09	6.7	2.16 × 1.73 (25)	0.91 × 0.75 (−5)	0.23 ± 0.06	5.6
17	143.108385	17_0-17_{-1} E, $v_t = 0$	366.8	6.44(−6)	2.06 × 1.67 (26)	0.61x0.50 (0)	0.52 ± 0.11	6.9	2.06 × 1.67 (26)	0.50	0.18 ± 0.04	6.9
18	166.773281	5_1-5_0 A^+, $v_t = 1$	390.0	1.85(−5)	2.54 × 1.71 (113)	0.91 × 0.46 (67)	0.90 ± 0.19	6.4	2.38 × 1.76 (114)	0.58	0.45 ± 0.10	7.5
19	165.074355	14_6-15_5 E1, $v_t = 0$	422.4	5.36(−6)	2.31 × 1.72 (110)	0.90 × 0.62 (37)	0.47 ± 0.10	5.5	2.39 × 1.77 (114)	2.02 × 1.01 (−53)	0.30 ± 0.06	6.0
20	144.750264	3_1-2_1 E2, $v_t = 1$	427.3	1.08(−5)	2.08 × 1.65 (30)	point	0.28 ± 0.06	7.2	2.16 × 1.73 (25)	0.15	0.12 ± 0.04	6.7
21	144.768193	3_0-2_0 A^+, $v_t = 1$	437.5	1.22(−5)	2.08 × 1.65 (30)	0.46 × 0.40 (49)	0.28 ± 0.06	6.8	2.16 × 1.73 (25)	1.23	0.09 ± 0.03	4.4
22	144.572025	3_0-2_0 A^+, $v_t = 2$	522.1	1.42(−5)	2.08 × 1.65 (30)	0.52	0.21 ± 0.04	6.3	2.16 × 1.73 (25)	1.61 × 1.03 (−60)	0.15 ± 0.04	5.5
	144.571262	3_2-2_2 E2, $v_t = 2$	658.8	6.74(−6)	⋯	⋯	⋯	⋯	⋯	⋯	⋯	⋯
23	144.583961	3_1-2_1 E2. $v_t = 2$	545.9	1.09(−5)	2.08 × 1.65 (30)	⋯	0.20 ± 0.04	4.0	2.16 × 1.73 (25)	⋯	0.15 ± 0.05	16.3
24	166.843662	11_2-10_3 E1, $v_t = 1$	553.0	1.19(−6)	2.54 × 1.71 (113)	0.48	0.07 ± 0.02	3.5	2.38 × 1.76 (114)	⋯	<0.04	⋯
25	164.299104	15_2-14_1 A^-, $v_t = 1$	576.0	1.44(−5)	2.31 × 1.72 (110)	0.94 × 0.64 (−86)	0.43 ± 0.10	5.5	2.39 × 1.77 (114)	1.95 × 0.94 (−83)	0.21 ± 0.05	3.6
26	142.276432	9_7-10_6 E2, $v_t = 1$	627.5	1.11(−6)	2.06 × 1.67 (26)	1.66 × 0.50 (−42)	0.03 ± 0.01	6.6	2.06 × 1.67 (26)	0.41	0.02 ± 0.01	4.8
27	144.281736	3_1-2_1 A^+, $v_t = 2$	696.6	1.07(−5)	2.08 × 1.65 (30)	point	0.08 ± 0.02	7.2	2.16 × 1.73 (25)	0.78	0.06 ± 0.03	5.3
28	144.530553	3_0-2_0 E1, $v_t = 2$	748.1	1.22(−5)	2.08 × 1.65 (30)	0.34	0.04 ± 0.01	4.0	2.16 × 1.73 (25)	1.15	0.05 ± 0.01	4.1
29	144.499723	3_1-2_1 E1, $v_t = 2$	812.8	1.05(−5)	2.08 × 1.65 (30)	0.96	0.03 ± 0.01	7.0	2.16 × 1.73 (25)	point	0.03 ± 0.02	5.7
30	164.486238	26_2-26_1 E2, $v_t = 0$	843.0	2.69(−5)	2.31 × 1.72 (110)	0.85 × 0.43 (38)	0.30 ± 0.07	5.8	2.39 × 1.77 (114)	1.25	0.26 ± 0.05	5.8

Table A1
(Continued)

					IRAS 2A				IRAS 4A			
N	Frequency (GHz)	Transition	E_{up} (K)	A_{ul} (s^{-1})	Beam Size ($''\times''$, ^{o})	Source Size[a] ($''\times''$, ^{o})	Flux[b] (Jy km s^{-1})	dV_W^c (km s^{-1})	Beam Size ($''\times''$, ^{o})	Source Size (PA)[a] ($''\times''$, ^{o})	Flux[b] (Jy km s^{-1})	dV_W [c] (km s^{-1})
31	144.195014	24_6-25_5 E2, $v_t = 0$	884.4	5.16(−6)	2.08 × 1.65 (30)	1.76 × 0.69 (−59)	0.05 ± 0.01	6.0	2.16 × 1.73 (25)	point	0.07 ± 0.03	5.9
32	144.437702	10_9-10_{a0} E2, $v_t = 1$	922.9	2.82(−6)	2.08 × 1.65 (30)	⋯	<0.05	⋯	2.16 × 1.73 (25)	1.39	0.04 ± 0.01	7.6
33	144.807264	11_9-11_{a0} E1, $v_t = 1$	948.3	4.94(−6)	2.08 × 1.65 (30)	⋯	<0.05	⋯	2.16 × 1.73 (25)	1.39 × 0.67 (−2)	0.07 ± 0.02	6.9
34	145.068727	19_5-20_6 E2, $v_t = 1$	985.9	8.88(−6)	2.08 × 1.65 (30)	1.33	0.07 ± 0.02	6.5	2.16 × 1.73 (25)	0.6	0.10 ± 0.04	7.0
35	163.526070	28_4-27_5 A^-, $v_t = 0$	1021.9	8.13(−6)	2.31 × 1.72 (110)	1	0.04 ± 0.02	4.7	2.39 × 1.77 (114)	point	0.10 ± 0.04	7.0
36	164.554640	28_4-27_5 A^+, $v_t = 0$	1021.9	8.28(−6)	2.31 × 1.72 (110)	2.57 × 1.42 (28)	0.08 ± 0.03	⋯	2.39 × 1.77 (114)	point	0.04 ± 0.02	5.7

Notes:

[a] Size of the best Gaussian fit to the visibilities. Gaussian fits were performed on the channel showing the peak emission. When an elliptical Gaussian fit was not successful, a circular Gaussian was attempted. Gaussian fits resulting in a size of 0″ are marked by "point." Lines dominated by a molecular outflow are marked by "outflow." See text for more details.

[b] Flux derived from a circular mask with a diameter equal to the major axis of the beam of the telescope given for each transition in the table. The errors on the fluxes were computed as the quadratic sum of the statistical error and the calibration uncertainty (about ∼20%).

[c] Non-deconvolved FWHM linewidths derived from a Gaussian fit of the WideX spectra toward the source positions.

Table A2
Same as Table A1 but for $^{13}CH_3OH$

					IRAS 2A				IRAS 4A			
N	Frequency (GHz)	Transition	E_{up} (K)	A_{ul} (s^{-1})	Beam Size ($''\times''$, ^{o})	Source Size ($''\times''$, ^{o})	Flux (Jy km s^{-1})	dV_W (km s^{-1})	Beam Size ($''\times''$, ^{o})	Source Size ($''\times''$, ^{o})	Flux (Jy km s^{-1})	dV_W (km s^{-1})
1	141.603710	3_0-2_0, A^+, $v_t = 0$	13.6	1.15(−5)	2.06 × 1.67 (26)	1.26 × 0.84 (−40)	0.142 ± 0.032	4.6	2.06 × 1.67 (26)	2.15 × 1.13 (−33)	0.099 ± 0.026	6.9
2	165.575639	2_1-2_0, E1, $v_t = 0$	27.9	2.37(−5)	2.54 × 1.71 (113)	0.48	0.167 ± 0.044	5.2	2.38 × 1.76 (114)	2.27 × 1.39 (−62)	0.167 ± 0.037	3.6
3	142.807657	3_1-2_1 A^-, $v_t = 0$	28.3	1.05(−5)	2.06 × 1.67 (26)	1.20 × 0.78 (18)	0.112 ± 0.026	6.6	2.06 × 1.67 (26)	point	0.069 ± 0.020	5.6
4	165.609427	3_1-3_0 E1, $v_t = 0$	34.6	2.36(−5)	2.54 × 1.71 (113)	0.56	0.293 ± 0.073	6.4	2.38 × 1.76 (114)	0.56	0.191 ± 0.042	5.6
5	165.690996	4_1-4_0 E1, $v_t = 0$	43.7	2.34(−5)	2.54 × 1.71 (113)	1.04 × 0.71 (83)	0.270 ± 0.068	5.0	2.38 × 1.76 (114)	0.91	0.172 ± 0.040	5.0
6	165.851224	5_1-5_0 E1, $v_t = 0$	55.0	2.33(−5)	2.54 × 1.71 (113)	0.5	0.294 ± 0.067	5.0	2.38 × 1.76 (114)	2.43 × 0.73 (−55)	0.165 ± 0.036	4.1
7	142.173740	5_2-6_1 E2, $v_t = 0$	60	4.85(−6)	2.06 × 1.67 (26)	1.25	0.033 ± 0.010	6.4	…	…	…	…
8	166.128782	6_1-6_0 E1, $v_t = 0$	68.6	2.32(−5)	2.54 × 1.71 (113)	0.99 × 0.42 (25)	0.327 ± 0.078	5.2	2.38 × 1.76 (114)	1.74 × 0.75 (−88)	0.166 ± 0.041	5.5
9	163.872900	7_0-6_1 E1, $v_t = 0$	76.5	9.91(−6)	2.31 × 1.72 (110)	point	0.156 ± 0.051	5.4	2.39 × 1.77 (114)	1.80 × 0.74 (−45)	0.151 ± 0.037	4.5
10	166.569486	7_1-7_0 E1, $v_t = 0$	84.5	2.31(−5)	2.54 × 1.71 (113)	0.99 × 0.95 (−68)	0.419 ± 0.093	6.6	2.38 × 1.76 (114)	1.60 × 1.11 (−60)	0.233 ± 0.050	5.6
11	142.896760	6_2-7_1 A^-, $v_t = 0$	85.4	5.31(−6)	2.06 × 1.67 (26)	2.24	0.085 ± 0.021	8.1	2.06 × 1.67 (26)	1.45 × 0.77 (0)	0.090 ± 0.023	7.5
12	165.280537	6_2-7_1 A^+, $v_t = 0$	85.4	7.77(−6)	2.54 × 1.71 (113)	point	0.067 ± 0.020	4.4	2.38 × 1.76 (114)	0.76	0.079 ± 0.018	8.4
13	164.531587	13_1-12_2 A^-, $v_t = 0$	222.3	9.96(−6)	2.31 × 1.72 (110)	1.01	0.121 ± 0.047	3.6	2.39 × 1.77 (114)	2.15	0.105 ± 0.028	4.2

Table A3
Same as Table A1 but for $HCOOCH_3$

					IRAS 2A				IRAS 4A			
N	Frequency (GHz)	Transition	E_{up} (K)	A_{ul} (s^{-1})	Beam Size (″×″, °)	Source Size (″×″, °)	Flux (Jy km s^{-1})	dV_W (km s^{-1})	Beam Size (″×″, °)	Source Size (″×″, °)	Flux (Jy km s^{-1})	dV_W (km s^{-1})
1	141.652995	E, $11_{2,9}$-$10_{2,8}$	43.2	4.06(−5)	2.06 × 1.67 (26)	point	0.090 ± 0.024	7.2	2.06 × 1.67 (26)	1.65 × 0.50 (−14)	0.112 ± 0.029	7.0
2	141.667012	A, $11_{2,9}$-$10_{2,8}$	43.2	4.06(−5)	2.06 × 1.67 (26)	0.2	0.069 ± 0.018	7.2	2.06 × 1.67 (26)	0.93	0.119 ± 0.027	6.6
3	143.234201	E, $12_{1,11}$-$11_{1,10}$	47.3	4.22(−5)	2.31 × 1.82 (26)	point	0.073 ± 0.028	5.8	2.31 × 1.82 (26)	0.44	0.091 ± 0.035	4.1
4	143.240505	A, $12_{1,11}$-$11_{1,10}$	47.3	4.23(−5)	2.31 × 1.82 (26)	point	0.072 ± 0.023	5.8	2.31 × 1.82 (26)	0.52	0.111 ± 0.036	4.1
5	142.733524	E, $13_{1,13}$-$12_{1,12}$	49.3	4.28(−5)	2.06 × 1.67 (26)	0.43	0.190 ± 0.042	7.5	2.06 × 1.67 (26)	1.13	0.195 ± 0.044	7.1
	142.735139	A, $13_{1,13}$-$12_{1,12}$	49.3	4.28(−5)	⋯	⋯	⋯	⋯	⋯	⋯	⋯	⋯
6	142.815476	E, $13_{0,13}$-$12_{0,12}$	49.3	4.28(−5)	2.06 × 1.67 (26)	0.30	0.211 ± 0.047	7.6	2.06 × 1.67 (26)	1.20 × 0.70 (32)	0.213 ± 0.050	8.3
	142.817021	A, $13_{0,13}$-$12_{0,12}$	49.3	4.28(−5)	⋯	⋯	⋯	⋯	⋯	⋯	⋯	⋯
7	142.924506	E, $13_{1,13}$-$12_{0,12}$	49.3	6.59(−6)	2.06 × 1.67 (26)	point	0.045 ± 0.012	8.8	2.06 × 1.67 (26)	point	0.112 ± 0.027	9.7
	142.925911	A, $13_{1,13}$-$12_{0,12}$	49.3	6.59(−6)	⋯	⋯	⋯	⋯	⋯	⋯	⋯	⋯
8	164.955703	E, $13_{2,11}$-$12_{2,10}$	58.5	6.46(−5)	2.31 × 1.72 (110)	0.85	0.159 ± 0.051	6.2	2.39 × 1.77 (114)	1.88	0.236 ± 0.058	5.5
9	164.968638	A, $13_{2,11}$-$12_{2,10}$	58.5	6.46(−5)	2.31 × 1.72 (110)	0.4	0.124 ± 0.039	3.5	2.39 × 1.77 (114)	0.38	0.209 ± 0.047	7.0
10	163.829677	E, $14_{1,13}$-$13_{1,12}$	62.5	6.37(−5)	2.31 × 1.72 (110)	1.13 × 0.46 (66)	0.131 ± 0.056	6.7	2.28 × 1.76	0.88	0.152 ± 0.048	4.7
11	163.835525	A, $14_{1,13}$-$13_{1,12}$	62.5	6.37(−5)	2.31 × 1.72 (110)	1.82 × 1.36 (14)	0.129 ± 0.039	3.6	2.28 × 1.76(−70)	1.64 × 0.73	0.149 ± 0.043	4.4
12	165.653657	E, $14_{2,13}$-$13_{1,12}$	62.6	7.63(−6)	2.54 × 1.71 (113)	1.6	0.057 ± 0.017	6.3	2.38 × 1.76 (114)	1.65	0.196 ± 0.026	14.3
	165.657529	A, $14_{2,13}$-$13_{1,12}$	62.6	7.63(−6)	⋯	⋯	⋯	⋯	⋯	⋯	⋯	⋯
13	163.925845	E, $15_{0,15}$-$14_{1,14}$	64.5	1.02(−5)	2.31 × 1.73	1.89 × 1.30 (28)	0.070 ± 0.033	7.8	2.39 × 1.77 (114) (−61)	2.40 × 0.86	0.141 ± 0.035	6.2
	163.927369	A, $15_{0,15}$-$14_{1,14}$	64.5	1.02(−5)	⋯	⋯	⋯	⋯	⋯	⋯	⋯	⋯
14	163.960387	A, $15_{1,15}$-$14_{1,14}$	64.5	6.53(−5)	2.31 × 1.72 (110)	1.48 × 0.56 (79)	0.301 ± 0.072	6.9	2.28 × 1.76	0.96	0.329 ± 0.080	5.9
	163.961884	E, $15_{1,15}$-$14_{1,14}$	64.5	6.53(−5)	⋯	⋯	⋯	⋯	⋯	⋯	⋯	⋯
15	163.987455	E, $15_{0,15}$-$14_{0,14}$	64.5	6.54(−5)	2.31 × 1.72 (110)	0.78 × 0.33 (19)	0.299 ± 0.072	6.9	2.22 × 1.94	0.93	0.086 ± 0.027	6.0
15	163.988912	A, $15_{0,15}$-$14_{0,14}$	64.5	6.54(−5)	⋯	⋯	⋯	⋯	2.22 × 1.94	0.55	0.136 ± 0.034	⋯
16	164.022026	E, $15_{1,15}$-$14_{0,14}$	64.5	1.03(−5)	2.31 × 1.72 (110)	1.81 × 0.76 (90)	0.118 ± 0.046	9.7	2.39 × 1.77 (114)	point	0.202 ± 0.065	10.0
	164.023416	A, $15_{1,15}$-$14_{0,14}$	64.5	1.03(−5)	⋯	⋯	⋯	⋯	⋯	⋯	⋯	⋯
17	164.205978	E, $13_{4,9}$-$12_{4,8}$	64.9	5.98(−5)	2.31 × 1.72 (110)	1.17	0.126 ± 0.039	5.9	2.28 × 1.76	0.65	0.193 ± 0.088	6.6
18	164.223815	A, $13_{4,9}$-$12_{4,8}$	64.9	5.98(−5)	2.31 × 1.72 (110)	1.29 × 0.90 (73)	0.138 ± 0.041	6.5	2.28 × 1.76 (0)	3.02 × 1.74	0.202 ± 0.074	5.2
19	142.664676	E, $12_{1,11}$-$11_{1,10}$, v_t =1	234.0	4.19(−5)	2.06 × 1.67 (26)	⋯	<0.040	⋯	2.06 × 1.67 (26)	2.65 × 2.24 (0)	0.037 ± 0.009	6.1
20	142.125411	E, $13_{0,13}$-$12_{0,12}$, v_t =1	236.9	4.24(−5)	2.06 × 1.67 (26)	1.19	0.033 ± 0.011	6.0	2.06 × 1.67 (26)	⋯	<0.048	⋯
21	142.052774	A, $13_{0,13}$-$12_{0,12}$, v_t =1	236.9	4.21(−5)	2.06 × 1.67 (26)	⋯	<0.040	⋯	2.06 × 1.67 (26)	2.24 × 0.56 (−29)	0.038 ± 0.018	8.1
22	166.388878	$13_{3,10}$-$12_{3,9}$, v_t=1	248.0	6.51(−5)	2.54 × 1.71 (113)	point	0.072 ± 0.032	5.1	2.63 × 1.73	⋯	<0.043	⋯

Table A4
Same as Table A1 but for CH_3CN

					IRAS 2A				IRAS 4A			
N	Frequency (GHz)	Transition	E_{up} (K)	A_{ul} (s^{-1})	Beam Size ($''\times''$, ^{o})	Source Size ($''\times''$, ^{o})	Flux (Jy km s^{-1})	dV_W (km s^{-1})	Beam Size ($''\times''$, ^{o})	Source Size ($''\times''$, ^{o})	Flux (Jy km s^{-1})	dV_W (km s^{-1})
1	165.569082	9_0-8_0	39.7	2.65(−4)	2.54 × 1.71 (113)	0.99 × 0.78 (45)	1.845 ± 0.373	10.2	2.38 × 1.76 (114)	1.68 × 1.27 (−67)	1.058 ± 0.217	9.4
	165.565891	9_1-8_1	46.9	2.62(−4)	…	…	…	…	…	…	…	…
2	165.556322	9_2-8_2	68.3	2.52(−4)	2.54 × 1.71 (113)	1.07 × 0.70 (−57)	0.818 ± 0.170	5.5	2.38 × 1.76 (114)	0.55	0.533 ± 0.116	5.1
3	165.540377	9_3-8_3	104.0	2.36(−4)	2.54 × 1.71 (113)	0.98 × 0.77 (65)	0.986 ± 0.205	6.1	2.38 × 1.76 (114)	0.51	0.493 ± 0.104	5.7
4	165.518064	9_4-8_4	154.0	2.13(−4)	2.54 × 1.71 (113)	0.87 × 0.79 (−26)	0.541 ± 0.116	6.1	2.38 × 1.76 (114)	1.22 × 0.5 (−56)	0.371 ± 0.081	6.0
5	165.489391	9_5-8_5	218.3	1.83(−4)	2.54 × 1.71 (113)	0.44	0.426 ± 0.097	6.8	2.38 × 1.76 (114)	0.52	0.482 ± 0.109	8.7
6	165.454370	9_6-8_6	296.8	1.47(−4)	2.54 × 1.71 (113)	0.74 × 0.45 (−80)	0.331 ± 0.078	6.6	2.38 × 1.76 (114)	1.29 × 0.65 (−74)	0.310 ± 0.070	5.3
7	165.413015	9_7-8_7	389.5	1.04(−4)	2.54 × 1.70	0.44	0.111 ± 0.049	6.4	2.38 × 1.76 (114)	1.88 × 0.75 (−20)	0.075 ± 0.032	4.8

Table A5
Same as Table A1 but for CH_3OCH_3

					IRAS 2A				IRAS 4A			
N	Frequency (GHz)	Transition	E_{up} (K)	A_{ul} (s^{-1})	Beam Size ($''\times''$, ^{o})	Source Size ($''\times''$, ^{o})	Flux (Jy km s^{-1})	dV_W (km s^{-1})	Beam Size ($''\times''$, ^{o})	Source Size ($''\times''$, ^{o})	Flux (Jy km s^{-1})	dV_W (km s^{-1})
1	143.017994	$3_{2,2}$-$2_{1,1}$, EA	11.1	1.09e-5	2.06 × 1.67 (26)	0.81	0.044 ± 0.023	10.1	2.06 × 1.67 (26)	3.81 × 1.66 (89)	0.060 ± 0.022	8.5
	143.018373	$3_{2,2}$-$2_{1,1}$, AE	11.1	1.09e-5	…	…	…	…	…	…	…	…
	143.020764	$3_{2,2}$-$2_{1,1}$, EE	11.1	1.09e-5	…	…	…	…	…	…	…	…
	143.023345	$3_{2,2}$-$2_{1,1}$, AA	11.1	1.09e-5	…	…	…	…	…	…	…	…
2	144.856766	$6_{3,3}$-$6_{2,4}$ EA	31.8	1.04(−5)	2.08 × 1.65 (30)	0.38	0.070 ± 0.016	5.1	2.16 × 1.73 (25)	1.29 × 1.28 (0)	0.161 ± 0.045	19.6
	144.858984	$6_{3,3}$-$6_{2,4}$ EE	31.8	1.06(−5)	…	…	…	…	…	…	…	…
	144.855091	$6_{3,3}$-$6_{2,4}$ AE	31.8	1.06(−5)	…	…	…	…	…	…	…	…
3	143.599420	$7_{3,4}$-$7_{2,5}$ AE	38.2	1.10(−5)	2.08 × 1.65 (30)	1.39 × 0.94 (−11)	0.083 ± 0.030	16.1	2.16 × 1.73 (25)	point	0.136 ± 0.044	14.0
	143.600084	$6_{3,3}$-$6_{2,4}$ EA	38.2	1.10(−5)	…	…	…	…	…	…	…	…
	143.602993	$6_{3,3}$-$6_{2,4}$ EE	38.2	1.10(−5)	…	…	…	…	…	…	…	…
	143.606232	$6_{3,3}$-$6_{2,4}$ AA	38.2	1.10(−5)	…	…	…	…	…	…	…	…
4	141.828855	$8_{3,5}$-$8_{2,6}$, AE	45.5	1.11e-5	2.06 × 1.67 (26)	0.65	0.149 ± 0.045	14.3	2.06 × 1.67 (26)	0.46	0.140 ± 0.049	16.7
	141.829146	$8_{3,5}$-$8_{2,6}$, EA	45.5	1.11e-5	…	…	…	…	…	…	…	…
	141.832261	$8_{3,5}$-$8_{2,6}$, EE	45.5	1.11e-5	…	…	…	…	…	…	…	…
	141.835521	$8_{3,5}$-$8_{2,6}$, AA	45.5	1.11e-5	…	…	…	…	…	…	…	…
5	143.159951	$13_{2,12}$-$13_{1,13}$, EA	88	7.75e-6	2.06 × 1.67 (26)	0.31	0.050 ± 0.012	7.1	2.06 × 1.67 (26)	point	0.079 ± 0.022	13.0
	143.159952	$13_{2,12}$-$13_{1,13}$, AE	88	7.75e-6	…	…	…	…	…	…	…	…
	143.162986	$13_{2,12}$-$13_{1,13}$, EE	88	7.75e-6	…	…	…	…	…	…	…	…
	143.166020	$13_{2,12}$-$13_{1,13}$, AA	88	7.75e-6	…	…	…	…	…	…	…	…
6	165.208844	$15_{3,13}$-$15_{2,14}$ EA	122	1.75(−5)	2.31 × 1.72 (110)	point	0.121 ± 0.046	13.8	2.39 × 1.77 (114)	2.47 × 1.20 (−26)	0.115 ± 0.025	9.5
	165.208848	$15_{3,13}$-$15_{2,14}$ AE	122	1.75(−5)	…	…	…	…	…	…	…	…
	165.211731	$15_{3,13}$-$15_{2,14}$ EE	122	1.75(−5)	…	…	…	…	…	…	…	…
	165.214617	$15_{3,13}$-$15_{2,14}$ AA	122	1.75(−5)	…	…	…	…	…	…	…	…
7	164.988708	$20_{3,18}$-$19_{4,15}$ AA	204	4.60(−6)	2.31 × 1.72 (110)	point	0.074 ± 0.033	5.5	2.39 × 1.77 (114)	…	<0.072	…
	164.990831	$20_{3,18}$-$19_{4,15}$ EE	204	4.60(−6)	…	…	…	…	…	…	…	…
	164.992951	$20_{3,18}$-$19_{4,15}$ EA	204	4.60(−6)	…	…	…	…	…	…	…	…
	164.992958	$20_{3,18}$-$19_{4,15}$ AE	204	4.60(−6)	…	…	…	…	…	…	…	…
8	142.403201	$25_{1,24}$-$25_{2,23}$, EA	313.5	1.57e-5	2.06 × 1.67 (26)	point	0.051 ± 0.013	7.2	2.06 × 1.67 (26)	0.41	0.035 ± 0.011	6.0
	142.403201	$25_{1,24}$-$25_{2,23}$, AE	313.5	1.57e-5	…	…	…	…	…	…	…	…
	142.404442	$25_{1,24}$-$25_{2,23}$, EE	313.5	1.57e-5	…	…	…	…	…	…	…	…
	142.405682	$25_{1,24}$-$25_{2,23}$, AA	313.5	1.57e-5	…	…	…	…	…	…	…	…

Table A6
Same as Table A1 but for C_2H_5OH

					IRAS 2A				IRAS 4A			
N	Frequency (GHz)	Transition	E_{up} (K)	A_{ul} (s^{-1})	Beam Size ($''\times''$, ^{o})	Source Size ($''\times''$, ^{o})	Flux (Jy km s^{-1})	dV_W (km s^{-1})	Beam Size ($''\times''$, ^{o})	Source Size ($''\times''$, ^{o})	Flux (Jy km s^{-1})	dV_W (km s^{-1})
1	142.285054	$9_{0,9,2}$-$8_{1,8,2}$	37.2	1.51(−5)	2.06 × 1.67 (26)	2.74 × 0.47 (1)	0.027 ± 0.011	4.1	2.06 × 1.67 (26)	0.52	0.045 ± 0.015	8.2
2	164.900973	$6_{0,6,1}$-$5_{1,4,0}$	78.8	1.22(−5)	2.31 × 1.72 (110)	⋯	<0.066	⋯	2.39 × 1.77 (114)	⋯	<0.072	⋯
3	144.057496	$13_{3,11,2}$-$13_{2,12,2}$	87.9	1.80(−5)	2.08 × 1.65 (30)	point	0.031 ± 0.010	⋯	2.16 × 1.73 (25)	point	0.067 ± 0.018	4.1
4	141.820317	$8_{1,7,0}$-$7_{1,6,0}$	88.8	2.46e-5	2.06 × 1.67 (26)	1.16	0.034 ± 0.013	4.1	2.06 × 1.67 (26)	point	0.039 ± 0.015	6.4
5	164.626167	$5_{4,1,0}$-$4_{3,1,1}$	88.8	2.06(−5)	2.31 × 1.72(110)	⋯	<0.066	⋯	2.39 × 1.77 (114)	⋯	<0.072	⋯
6	164.630894	$5_{4,2,0}$-$4_{3,2,1}$	88.8	2.06(−5)	2.31 × 1.72 (110)	⋯	<0.066	⋯	2.39 × 1.77 (114)	⋯	<0.081	⋯
7	144.493107	$14_{2,13,2}$-$14_{11,4,2}$	92.6	1.86(−5)	2.08 × 1.65 (30)	⋯	<0.046	⋯	2.16 × 1.73 (25)	1.19	0.045 ± 0.021	4.1
8	166.259891	$10_{1,10,0}$-$9_{1,9,0}$	102.1	4.03(−5)	2.54 × 1.71 (113)	point	0.114 ± 0.049	7.3	2.38 × 1.76 (114)	1.08	0.118 ± 0.053	4.2
9	166.758214	$10_{1,10,1}$-$9_{1,9,1}$	106.8	4.07(−5)	2.54 × 1.71 (113)	0.95	0.043 ± 0.030	⋯	2.38 × 1.76 (114)	point	0.053 ± 0.020	⋯
10	142.083012	$11_{2,10,1}$-$11_{1,10,0}$	121	9.96(−6)	2.06 × 1.67 (26)	point	0.028 ± 0.009	16.3	2.06 × 1.67 (26)	⋯	<0.040	⋯
11	164.511879	$18_{3,15,2}$-$17_{4,14,2}$	156.8	8.73(−6)	2.31 × 1.72 (110)	point	0.036 ± 0.021	3.6	2.39 × 1.77 (114)	⋯	<0.072	⋯
12	164.429108	$14_{3,12,1}$-$13_{4,10,0}$	160.0	4.25(−6)	2.31 × 1.72 (110)	⋯	<0.066	⋯	2.39 × 1.77 (114)	⋯	<0.072	⋯
13	142.046310	$20_{2,18,2}$-$20_{1,19,2}$	185.5	1.77(−5)	2.06 × 1.67 (26)	⋯	<0.040	⋯	2.06 × 1.67 (26)	⋯	<0.040	⋯
13	163.515766	$21_{3,19,2}$-$20_{4,16,2}$	205.4	9.22(−6)	2.31 × 1.72 (110)	⋯	<0.066	⋯	2.39 × 1.77 (114)	⋯	<0.072	⋯
14	141.735490	$21_{4,17,2}$-$21_{3,18,2}$	215.5	1.72e-5	2.06 × 1.67 (26)	point	0.030 ± 0.015	8.0	2.06 × 1.67 (26)	point	0.048 ± 0.018	7.6

Table A7
Same as Table A1 but for $HCOCH_2OH$

					IRAS 2A				IRAS 4A			
N	Frequency (GHz)	Transition	E_{up} (K)	A_{ul} (s^{-1})	Beam Size ($''\times''$, ^{o})	Source Size ($''\times''$, ^{o})	Flux (Jy km-s)	dV_W (km s^{-1})	Beam Size ($''\times''$, ^{o})	Source Size ($''\times''$, ^{o})	Flux (Jy km-s)	dV_W (km s^{-1})
1	163.951686	$8_{3,5}$-$7_{2,6}$, $v = 0$	25.6	3.68(−5)	2.31 × 1.72 (110)	⋯	<0.066	⋯	2.39 × 1.77 (114)	⋯	⋯	⋯
2	143.640947	$14_{0,14}$-$13_{1,13}$, $v = 0$	53.1	8.04(−5)	2.08 × 1.65 (30)	point	0.037 ± 0.020	⋯	2.06 × 1.67 (26)	⋯	<0.129	⋯
3	143.765755	$14_{1,14}$-$13_{0,13}$, $v = 0$	53.1	8.06(−5)	2.08 × 1.65 (30)	⋯	<0.046	⋯	2.06 × 1.67 (26)	point	0.069 ± 0.035	5.6
4	164.047038	$15_{2,14}$-$14_{1,13}$, $v = 0$	66.5	9.25(−5)	2.31 × 1.72 (110)	point	0.076 ± 0.034	7.4	2.39 × 1.77 (114)	1.89	0.132 ± 0.051	4.5
5	163.542260	$16_{0,16}$-$15_{1,15}$, $v = 0$	68.3	1.21(−4)	2.31 × 1.72 (110)	point	0.037 ± 0.023	7.8	2.39 × 1.77 (114)	⋯	0.172 ± 0.050	8.0
6	163.580057	$16_{1,16}$-$15_{0,15}$, $v = 0$	68.3	1.21(−4)	2.31 × 1.72 (110)	point	0.038 ± 0.021	8.5	2.39 × 1.77 (114)	point	0.103 ± 0.038	5.0
7	163.697251	$12_{7,5}$-$12_{6,6}$, $v = 0$	73.1	5.60(−5)	2.31 × 1.72 (110)	⋯	<0.066	⋯	2.39 × 1.77 (114)	point	0.071 ± 0.028	3.6
8	163.709163	$12_{7,6}$-$12_{6,7}$, $v = 0$	73.1	5.60(−5)	2.31 × 1.72 (110)	⋯	<0.066	⋯	2.39 × 1.77 (114)	1.55	0.076 ± 0.045	3.8
9	142.784665	$23_{6,18}$-$23_{5,19}$	177	5.19(−5)	2.08 × 1.65 (30)	⋯	<0.040	⋯	2.06 × 1.67 (26)	point	0.039 ± 0.014	5.2

Table A8
Same as Table A1 but for C_2H_5CN

					IRAS 2A				IRAS 4A			
N	Frequency (GHz)	Transition	E_{up} (K)	A_{ul} (s^{-1})	Beam Size ($''\times''$, ^{o})	Source Size ($''\times''$, ^{o})	Flux (Jy km s^{-1})	dV_W (km s^{-1})	Beam Size ($''\times''$, ^{o})	Source Size ($''\times''$, ^{o})	Flux (Jy km s^{-1})	dV_W (km s^{-1})
1	142.346330	$16_{2,15}$-$15_{2,14}$	62.7	2.37(−4)	2.06 × 1.67 (26)	2.33	0.029 ± 0.010	12.0	2.06 × 1.67 (26)	2.51 × 1.17 (−40)	0.045 ± 0.013	6.8
2	143.529200	$16_{3,14}$-$15_{3,13}$	68.5	2.39(−4)	2.08 × 1.65 (30)	point	0.025 ± 0.009	4.1	2.16 × 1.73 (25)	⋯	<0.081	⋯
3	144.104740	$16_{3,13}$-$15_{3,12}$	68.6	2.42(−4)	2.08 × 1.65 (30)	⋯	<0.046	⋯	2.16 × 1.73 (25)	⋯	<0.081	⋯
4	143.506970	$16_{4,13}$-$15_{4,12}$	76.3	2.32(−4)	2.08 × 1.65 (30)	⋯	<0.046	⋯	2.16 × 1.73 (25)	⋯	<0.081	⋯
5	143.535290	$16_{4,12}$-$15_{4,11}$	76.3	2.32(−4)	2.08 × 1.65 (30)	⋯	<0.046	⋯	2.16 × 1.73 (25)	⋯	<0.081	⋯
6	164.584755	$19_{0,19}$-$18_{0,18}$	80	3.74(−4)	2.31 × 1.72 (110)	⋯	<0.066	⋯	2.39 × 1.77 (114)	⋯	<0.072	⋯
8	163.948705	$19_{1,19}$-$18_{1,18}$	80.1	3.69(−4)	2.31 × 1.72 (110)	⋯	<0.066	⋯	2.39 × 1.77 (114)	point	0.110 ± 0.044	8.5
7	143.406554	$16_{5,12}$-$15_{5,11}$	86.3	2.23(−4)	2.08 × 1.65 (30)	point	0.024 ± 0.016	5.8	2.16 × 1.73 (25)	⋯	<0.081	⋯
	143.407188	$16_{5,11}$-$15_{5,10}$	86.3	2.23(−4)	2.08 × 1.65 (30)	⋯	⋯	⋯	⋯	⋯	⋯	⋯
9	143.335284	$16_{8,8}$-$15_{8,7}$	129.6	1.85(−4)	2.06 × 1.67 (26)	point	0.045 ± 0.011	7.4	2.06 × 1.67 (26)	0.17	0.037 ± 0.012	11.2
	143.335284	$16_{8,9}$-$15_{8,8}$	129.6	1.85(−4)	⋯	⋯	⋯	⋯	⋯	⋯	⋯	⋯
	143.337710	$16_{7,10}$-$15_{7,9}$	112.9	1.99(−4)	⋯	⋯	⋯	⋯	⋯	⋯	⋯	⋯
	143.337710	$16_{7,9}$-$15_{7,8}$	112.9	1.99(−4)	⋯	⋯	⋯	⋯	⋯	⋯	⋯	⋯
10	143.343925	$16_{9,7}$-$15_{9,6}$	148.4	1.68(−4)	2.06 × 1.67 (26)	point	0.034 ± 0.010	7.1	2.06 × 1.67 (26)	1.43	0.045 ± 0.012	4.1
	143.343925	$16_{9,8}$-$15_{9,7}$	148.4	1.68(−4)	⋯	⋯	⋯	⋯	⋯	⋯	⋯	⋯

Table A9
Same as Table A1 but for other Molecules

Molecule	Frequency (GHz)	Transition	E_{up} (K)	A_{ul} (s^{-1})	IRAS 2A				IRAS 4A			
					Beam Size ($''\times''$, ^{o})	Source Size ($''\times''$, ^{o})	Flux (Jy km s^{-1})	dV_W (km s^{-1})	Beam Size ($''\times''$, ^{o})	Source Size ($''\times''$, ^{o})	Flux (Jy km s^{-1})	dV_W (km s^{-1})
HC_3N	163.753389	18–17	74.7	3.45(−4)	2.31 × 1.72 (110)	2.66 × 1.80 (34)	0.572 ± 0.116	6.2	2.39 × 1.77 (114)	6.03 × 1.96 (17)	0.553 ± 0.121	7.4
$H_2^{13}CO$	141.98374	$2_{0,2}$-$1_{0,1}$	10.2	7.25(−5)	2.06 × 1.67 (26)	0.60	0.115 ± 0.028	6.3	2.06 × 1.67 (26)	2.45 × 1.25 (0)	0.062 ± 0.022	7.3
$H_2C^{18}O$	143.213062	$2_{1,1}$-$1_{1,0}$	22.2	5.57(−5)	2.06 × 1.67 (26)	1.94 × 1.05 (1)	0.028 ± 0.007	…	…	…	…	…
NH_2CHO	142.701479	$7_{7,1,7,8}$-$6_{1,6,7}$	30.4	2.02(−4)	2.06 × 1.67 (26)	point	0.185 ± 0.043	8.2	2.06 × 1.67 (26)	point	0.090 ± 0.025	7.4
CH_2CO	142.76892	$7_{1,6}$-$6_{1,5}$	40.5	3.10(−5)	2.06 × 1.67 (26)	1.03 × 0.61 (30)	0.119 ± 0.028	5.8	2.06 × 1.67 (26)	1.80 × 1.34 (34)	0.184 ± 0.040	5.1

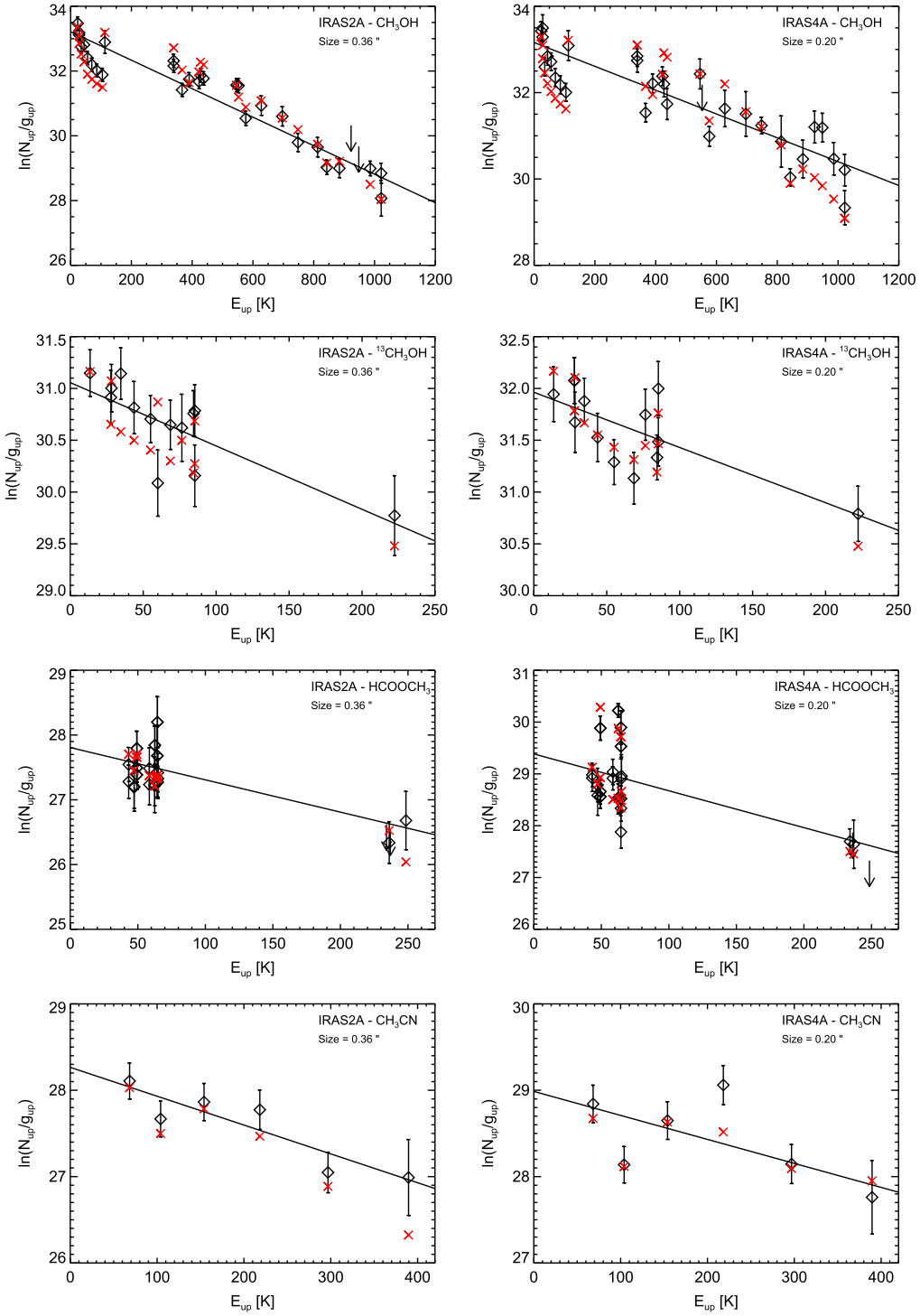

Figure A1. Rotational and population diagrams of methanol isotopologues (CH_3OH, $^{13}CH_3OH$), $HCOOCH_3$, and CH_3CN for source sizes derived from the PD analysis of the methanol population distribution (0.″36 for IRAS 2A and 0.″20 for IRAS 4A). Observational data is depicted by the black diamonds. Error bars are derived assuming a calibration uncertainty of 20% on top of the statistical error. Straight lines represent the best fit of the RD analysis to the data. Red crosses show the best fit of the PD to the data.

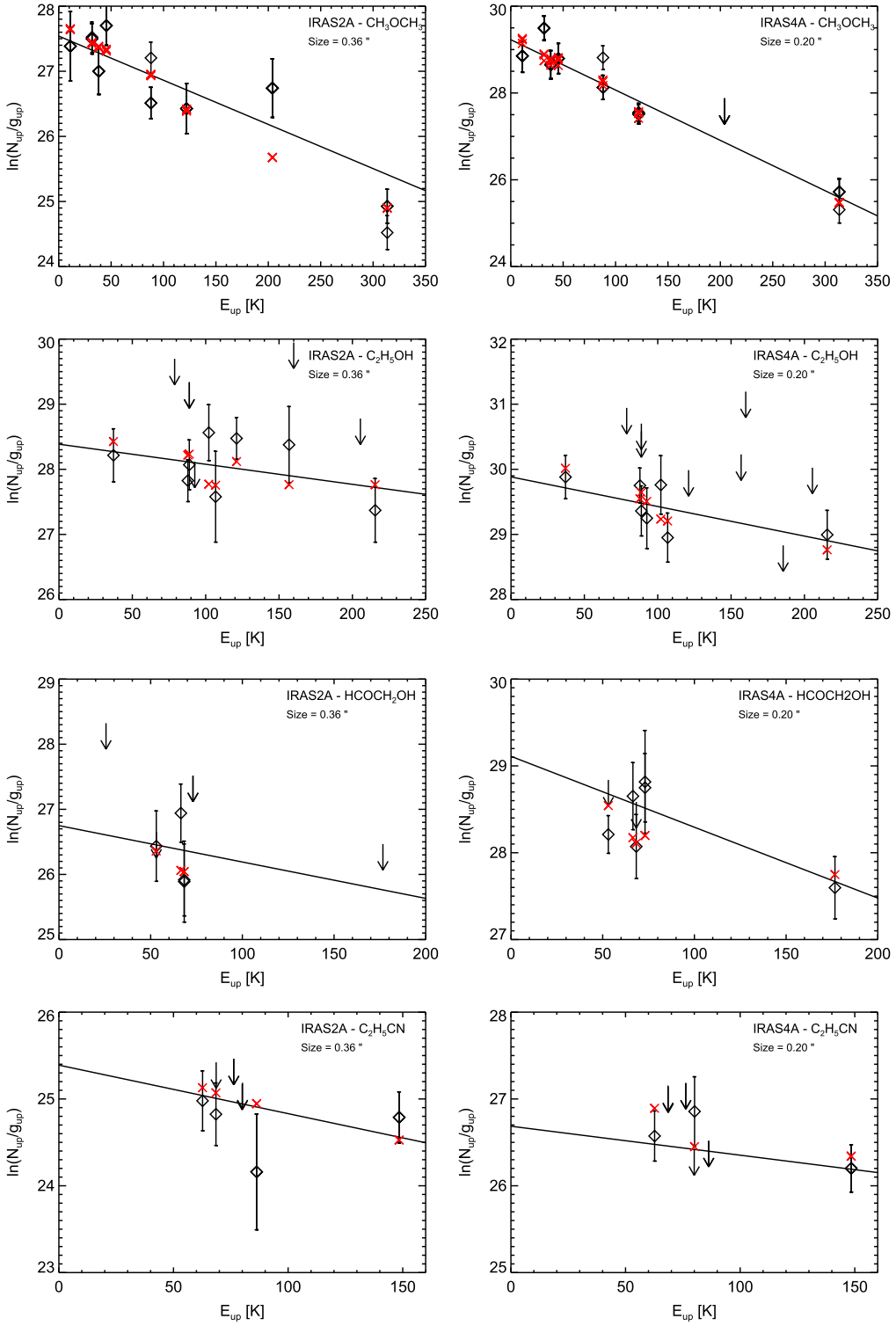

Figure A2. Rotational and population diagrams of CH_3OCH_3, C_2H_5OH, $HCOCH_2OH$, C_2H_5CN for source sizes derived from the PD analysis of the methanol population distribution (0.″36 for IRAS 2A and 0.″20 for IRAS 4A). Observational data is depicted by the black diamonds. Error bars are derived assuming a calibration uncertainty of 20% on top of the statistical error. Straight lines represent the best fit of the RD analysis to the data. Red crosses show the best fit of the PD to the data.

Table A10
COM Abundances Observed in High-mass, Intermediate-mass, and Low-mass Hot Cores

Source	L_{bol} ($L_\odot$)	$N(H_2)$ (cm^{-2})	CH_3OH T_{rot} (K)	CH_3OH X_{H2}	H_2CO X_{meth}	CH_2CO X_{meth}	$HCOOCH_3$ X_{meth}	$HCOCH_2OH$ X_{meth}	CH_3OCH_3 X_{meth}	C_2H_5OH X_{meth}	CH_3CN X_{meth}	C_2H_5CN X_{meth}	Reference
High-mass Protostars Observed With Single-dish Telescopes													
IRAS20126 + 4104	1.3(+4)	1.0(+24)	300	1.1(−7)	2.9(−1)	<1.1(−2)	<1.8(−2)	⋯	<9.1(−2)	<2.7(−2)	5.2(−2)	<4.5(−3)	1
IRAS18089–1732	3.2(+4)	1.0(+24)	300	2.0(−7)	8.6(−2)	3.1(−2)	1.3(−1)	⋯	5.9(−1)	1.8(−1)	2.1(−2)	1.4(−2)	1
G31.41 + 0.31	2.6(+5)	1.7(+23)	200	6.0(−6)	5.4(−2)	2.8(−2)	1.4(−1)	1.1(−1)	4.5(−1)	1.3(−1)	1.3(−2)	1.7(−2)	1
AFGL 2591	2.0(+4)	7.6(+22)	147	6.2(−7)	2.8(−1)	2.1(−2)	<5.1(−1)	⋯	<1.6(−1)	<2.1(−2)	<7.4(−2)	<1.6(−2)	2
NGC 7538 IRS1	1.3(+5)	2.1(+23)	156	5.7(−7)	2.1(−1)	5.3(−2)	1.2(−1)	⋯	<1.3(−1)	4.8(−2)	<6.8(−2)	<7.7(−3)	2
G24.78	7.9(+5)	4.0(+23)	211	7.0(−7)	2.3(−1)	5.2(−2)	1.1(−1)	⋯	4.3(−1)	2.5(−2)	2.1(−1)	1.4(−2)	2
G75.78	1.9(+5)	1.2(+23)	113	9.2(−7)	2.0(−1)	6.2(−2)	6.5(−2)	⋯	2.1(−1)	<2.2(−2)	1.6(−2)	<1.1(−2)	2
W33A	1.0(+5)	2.6(+23)	259	7.7(−7)	2.7(−1)	4.9(−2)	1.3(−1)	⋯	1.4(−1)	2.4(−2)	1.4(−1)	<1.1(−2)	2
NGC 6334 IRS1	1.7(+5)	2.4(+23)	178	4.0(−6)	1.3(−1)	2.0(−2)	1.2(−1)	⋯	6.0(−1)	2.0(−2)	3.0(−2)	5.3(−3)	2
W3 (H2O)	2.0(+4)	1.8(+23)	181	5.6(−6)	1.8(−1)	1.5(−2)	5.2(−2)	⋯	1.5(−1)	8.4(−3)	7.0(−3)	4.5(−3)	2
Sgr B2 (M)	6.5(+6)	3.5(+24)	150	7.4(−9)	1.0(−1)	1.9(−2)	6.2(−2)	⋯	⋯	4.2(−2)	6.0(−2)	⋯	3
Sgr B2 (N)	6.5(+6)	8.0(+24)	170	6.3(−7)	4.8(−2)	1.4(−2)	<3.8(−2)	⋯	5.6(−2)	3.8(−2)	5.1(−2)	1.3(−1)	4
G327.3–0.6	1.0(+5)	3.0(+24)	118	2.0(−5)	3.6(−5)	⋯	8.0(−2)	⋯	5.4(−1)	4.1(−3)	3.5(−2)	2.2(−2)	5
Orion KL—HC	1.0(+5)	3.1(+23)	128	2.2(−6)	5.5(−2)	⋯	⋯	⋯	3.1(−2)	⋯	1.4(−2)	5.0(−3)	6
Orion KL—CR	1.0(+5)	3.9(+23)	140	1.2(−6)	3.7(−2)	4.3(−3)	2.8(−1)	⋯	1.4(−1)	1.4(−2)	1.1(−2)	⋯	6
G34.3 + 0.15	6.3(+5)	5.3(+23)	336	7.0(−8)	⋯	1.8(−2)	4.3(−1)	⋯	2.5(−1)	9.5(−2)	6.5(−3)	⋯	7
G34.3 + 0.2	6.3(+5)	1.6(+23)	96	1.7(−7)	⋯	⋯	5.4(−2)	⋯	1.4(−1)	6.5(−2)	⋯	1.0(−2)	8
DR21(OH)	5.0(+4)	2.5(+24)	150	1.0(−8)	⋯	⋯	<4.0(−3)	⋯	⋯	<5.2(−3)	⋯	<8.4(−4)	8
W51	1.5(+6)	3.3(+23)	208	3.0(−7)	⋯	⋯	1.2(−1)	⋯	⋯	3.1(−2)	⋯	7.0(−3)	8
High-mass Hot Cores Observed With Interferometers													
Orion KL	1.0(+5)	4.4(+24)	200	4.5(−9)	⋯	⋯	3.0(−1)	⋯	5.0(−1)	1.0(−1)	1.0(−1)	2.5(−1)	9
G29.96	9.0(+4)	3.3(+24)	200	1.2(−7)	⋯	⋯	2.0(−1)	⋯	5.0(−1)	1.5(−1)	2.5(−2)	2.5(−2)	10
G19.61–0.23	1.6(+5)	8.4(+23)	151	6.2(−7)	⋯	⋯	4.2(−2)	⋯	2.7(−2)	1.2(−1)	7.9(−2)	3.1(−2)	11
Intermediate-mass Hot Cores Observed With Interferometers													
I22198-MM2	370	2.0(+25)	120	1.2(−6)	⋯	⋯	1.1(−2)	⋯	⋯	9.1(−3)	⋯	⋯	12
A5142-MM1	2300	1.0(+25)	210	2.3(−7)	⋯	⋯	<8.7(−2)	⋯	⋯	9.1(−2)	⋯	⋯	12
A5142-MM2	2300	2.0(+25)	140	2.0(−7)	⋯	⋯	<5.0(−2)	⋯	⋯	2.0(−2)	⋯	⋯	12
NGC 7129 FIRS2	500	2.5(+24)	238	1.0(−6)	1.6(−2)	⋯	1.5(−2)	⋯	1.2(−2)	8.8(−3)	5.2(−3)	3.5(−4)	13
Low-mass Protostars Observed With Single-dish Telescopes													
IRAS 16293	27	2.0(+23)	84	1.0(−7)	2.6(−1)	1.0(−3)	9.0(−2)	6.9(−3)	4.0(−1)	<5.0(−2)	9.1(−3)	<2.0(−3)	14
IRAS 2A	36	2.1(+23)	101	8.8(−7)	2.9(−1)	⋯	<8.5(−1)	⋯	<5.3(−1)	⋯	1.1(−2)	<1.3(−1)	15
IRAS 4A	9.1	1.6(+24)	24	1.4(−7)	1.4(−1)	⋯	5.5(−1)	⋯	<2.2(−1)	⋯	1.3(−2)	<9.2(−3)	15
IRAS4B	4.4	8.1(+22)	34	6.9(−6)	2.0(−1)	⋯	1.3(−1)	⋯	<1.9(−1)	⋯	1.6(−2)	<1.2(−1)	15
SMM1	30	1.3(+23)	16	1.9(−9)	⋯	⋯	1.0(−1)	⋯	5.3(−2)	<3.4(−2)	⋯	⋯	16
SMM4	1.9	1.1(+23)	13	9.5(−9)	⋯	⋯	<1.0(−2)	⋯	<8.0(−3)	<6.0(−3)	⋯	⋯	16
B1-a	1.3	1.9(+22)	15	6.4(−10)	⋯	⋯	1.0(−1)	⋯	<6.7(−2)	⋯	1.3(−2)	⋯	17
SVS 4–5	38	5.7(+22)	20	3.9(−9)	⋯	⋯	4.5(−2)	⋯	1.0(−1)	⋯	7.7(−3)	⋯	17

Table A10
(Continued)

Source	L_{bol} ($L_\odot$)	$N(H_2)$ (cm^{-2})	CH_3OH T_{rot} (K)	CH_3OH X_{H2}	H_2CO X_{meth}	CH_2CO X_{meth}	$HCOOCH_3$ X_{meth}	$HCOCH_2OH$ X_{meth}	CH_3OCH_3 X_{meth}	C_2H_5OH X_{meth}	CH_3CN X_{meth}	C_2H_5CN X_{meth}	Reference
B5 IRS1	4.7	2.3(+22)	17	1.0(−9)	⋯	⋯	<1.7(−1)	⋯	<3.5(−1)	⋯	1.7(−2)	⋯	17
IRAS03235	1.9	1.4(+23)	18	8.6(−11)	⋯	⋯	<1.7(−1)	⋯	<4.2(−1)	⋯	<2.5(−2)	⋯	17
IRAS04108	0.62	2.9(+22)	9	4.1(−10)	⋯	⋯	<8.3(−2)	⋯	⋯	⋯	⋯	⋯	17
L1489 IRS	3.7	4.3(+22)	8	1.2(−10)	⋯	⋯	<4.0(−1)	⋯	⋯	⋯	⋯	⋯	17
Low-mass Hot Corinos Observed With Interferometers													
IRAS 2A-RD	36	2.0(+24)	179	2.5(−7)	8.1(−2)	1.4(−3)	1.9(−2)	1.5(−3)	1.2(−2)	1.5(−2)	3.0(−3)	2.7(−4)	18
IRAS 2A-PD	36	2.0(+24)	140	1.0(−6)	⋯	⋯	1.6(−2)	1.4(−3)	1.0(−2)	1.6(−2)	4.0(−3)	3.0(−4)	18
IRAS 4A-RD	9.1	1.4(+25)	300	1.7(−8)	6.3(−2)	2.8(−3)	1.5(−2)	2.5(−3)	8.7(−3)	1.2(−2)	1.8(−3)	4.2(−4)	18
IRAS 4A-PD	9.1	1.4(+25)	140	4.3(−7)	⋯	⋯	3.1(−2)	3.0(−3)	1.0(−2)	1.0(−2)	3.9(−3)	4.0(−4)	18

Reference. (1) Isokoski et al. (2013), (2) Bisschop et al. (2007), (3) Nummelin et al. (2000), (4) Neill et al. (2014), (5) Gibb et al. (2000), (6) Crockett et al. (2014), (7) MacDonald et al. (1996), (8) Ikeda et al. (2001), (9) Beuther et al. (2009), (10) Beuther et al. (2007), (11) Qin et al. (2010), (12) Palau et al. (2011), (13) Fuente et al. (2014), (14) Maret et al. (2005), Jaber et al. (2014), (15) Maret et al. (2004, 2005), Bottinelli et al. (2004a, 2007), (16) Öberg et al. (2011), (17) Öberg et al. (2014). (18) This work

REFERENCES

Aikawa, Y., Wakelam, V., Garrod, R. T., & Herbst, E. 2008, ApJ, 674, 984
Alekseev, E. A., Dyubko, S. F., Ilyushin, V. V., & Podnos, S. V. 1996, JMoSp, 176, 316
Allamandola, L. J., Sandford, S. A., & Valero, G. J. 1988, Icar, 76, 225
Anderson, T., Crownover, R. L., Herbst, E., & DeLucia, F. C. 1988, ApJS, 67, 135
Arce, H. G., Santiago-García, J., Jørgensen, J. K., et al. 2008, ApJL, 681, L21
Bacmann, A., Taquet, V., Faure, A., et al. 2012, A&A, 541, L12
Balucani, N., Ceccarelli, C., & Taquet, V. 2015, MNRAS, 449, L16
Beuther, H., Zhang, Q., Bergin, E. A., et al. 2007, A&A, 468, 1045
Beuther, H., Zhang, Q., Bergin, E. A., & Sridharan, T. K. 2009, AJ, 137, 406
Bisschop, S. E., Jørgensen, J. K., Bourke, T. L., et al. 2008, A&A, 488, 959
Bisschop, S. E., Jørgensen, J. K., van Dishoeck, E. F., & de Wachter, E. B. M. 2007, A&A, 465, 913
Blake, G. A., Sutton, E. C., Masson, C. R., & Phillips, T. G. 1987, ApJ, 315, 621
Bogey, M., Demuynck, C., & Destombes, J. L. 1982, JMoSp, 95, 35
Boogert, A. C. A., Blake, G. A., & Tielens, A. G. G. M. 2002, ApJ, 577, 271
Bottinelli, S., Ceccarelli, C., Lefloch, B., et al. 2004a, ApJ, 615, 354
Bottinelli, S., Ceccarelli, C., Neri, R., et al. 2004b, ApJL, 617, L69
Bottinelli, S., Ceccarelli, C., Williams, J. P., & Lefloch, B. 2007, A&A, 463, 601
Carrol, P., Drouin, B. J., & Weaver, S. L. W. 2010, ApJ, 723, 845
Caux, E., Kahane, C., Castets, A., Coutens, A., Ceccarelli, C., et al. 2011, A&A, 532, A23
Cazaux, S., Tielens, A. G. G. M., Ceccarelli, C., et al. 2003, ApJL, 593, L51
Cazzoli, G., & Puzzarini, C. 2006, JMoSp, 240, 153
Cernicharo, J., Marcelino, N., Roueff, E., et al. 2012, ApJL, 759, L43
Charnley, S. B., Tielens, A. G. G. M., & Millar, T. J. 1992, ApJL, 399, L71
Choi, M. 2005, ApJ, 630, 976
Cohen, E. A., & Pickett, H. M. 1982, JMoSp, 93, 83
Coutens, A., Persson, M. V., Jørgensen, J. K., Wampfler, S. F., & Lykke, J. M. 2015, A&A, 576, A5
Crockett, N. R., Bergin, E. A., Neill, J. L., et al. 2014, ApJ, 787, 112
Dangoisse, D., Willemot, E., & Bellet, J. 1978, JMoSp, 71, 414
De Lucia, F. C., & Gordy, W. 1969, PhRv, 187, 58
Endres, C. P., Drouin, B. J., Pearson, J. C., et al. 2009, A&A, 504, 635
Fabricant, B., Krieger, D., & Muenter, J. S. 1977, JChPh, 67, 1576
Fuente, A., Cernicharo, J., Caselli, P., et al. 2014, A&A, 568, A65
Fukuyama, Y., Odashima, H., Takagi, K., & Tsunekawa, S. 1996, ApJS, 104, 329
Garrod, R. T. 2013, ApJ, 765, 60
Garrod, R. T., & Herbst, E. 2006, A&A, 457, 927
Garrod, R. T., Weaver, S. L. W., & Herbst, E. 2008, ApJ, 682, 283
Geppert, W. D., Hamberg, M., Thomas, R. D., et al. 2006, FaDi, 133, 177
Gerakines, P. A., Schutte, W. A., & Ehrenfreund, P. 1996, A&A, 312, 289
Gibb, E., Nummelin, A., Irvine, W. M., et al. 2000, ApJ, 545, 309
Goldsmith, P. F., & Langer, W. D. 1999, ApJ, 517, 209
Hamberg, M., Österdahl, F., Thomas, R. D., et al. 2010, A&A, 514, A83
Herbst, E., & van Dishoeck, E. F. 2009, ARA&A, 47, 427
Hirota, T., Bushimata, T., Choi, Y. K., et al. 2008, PASJ, 60, 37
Hollis, J. M., Lovas, F. J., & Jewell, P. R. 2000, ApJL, 540, L107
Hollis, J. M., Vogel, S. N., Snyder, L. E., Jewell, P. R., & Lovas, F. J. 2001, ApJL, 554, L81
Horn, A., Møllendal, H., Sekiguchi, O., et al. 2004, ApJ, 611, 605
Hudson, R. L., & Moore, M. H. 2000, Icar, 145, 661
Ikeda, M., Ohishi, M., Nummelin, A., et al. 2001, ApJ, 560, 792
Ilyushin, V., Kryvda, A., & Alekseev, E. 2009, JMoSp, 255, 32
Isokoski, K., Bottinelli, S., & van Dishoeck, E. F. 2013, A&A, 554, A100
Jaber, A. A., Ceccarelli, C., Kahane, C., & Caux, E. 2014, ApJ, 791, 29
Johnson, D. R., Lovas, F. J., & Kirchhoff, W. H. 1972, JPCRD, 1, 1011
Jørgensen, J. K., Bourke, T. L., Myers, P. C., et al. 2005, ApJ, 632, 973
Jørgensen, J. K., Bourke, T. L., Myers, P. C., et al. 2007, ApJ, 659, 479
Jørgensen, J. K., Bourke, T. L., Nguyen Luong, Q., & Takakuwa, S. 2011, A&A, 534, A100
Jørgensen, J. K., Favre, C., Bisschop, S. E., et al. 2012, ApJL, 757, L4
Karska, A., Herczeg, G. J., van Dishoeck, E. F., et al. 2013, A&A, 552, A141
Kristensen, L. E., van Dishoeck, E. F., Bergin, E. A., et al. 2012, A&A, 542, A8
Kuan, Y.-J., Huang, H.-C., Charnley, S. B., et al. 2004, ApJL, 616, L27
Lafferty, W. J., & Lovas, F. J. 1978, JPCRD, 7, 441
Looney, L. W., Mundy, L. G., & Welch, W. J. 2000, ApJ, 529, 477
Lovas, F. J., Lutz, H., & Dreizler, H. 1979, JPCRD, 8, 1051
MacDonald, G. H., Gibb, A. G., Habing, R. J., & Millar, T. J. 1996, A&AS, 119, 333
Maret, S., Ceccarelli, C., Caux, E., et al. 2004, A&A, 416, 577
Maret, S., Ceccarelli, C., Tielens, A. G. G. M., et al. 2005, A&A, 442, 527
Maury, A. J., Belloche, A., André, P., et al. 2014, A&A, 563, L2
Messer, J. K., DeLucia, F. C., & Helminger, P. 1984, JMoSp, 105, 139
Milam, S. N., Savage, C., Brewster, M. A., et al. 2005, ApJ, 634, 1126
Millar, T. J., Herbst, E., & Charnley, S. B. 1991, ApJ, 369, 147
Müller, H. S. P., Gendriesch, R., Margulès, L., Lewen, F., et al. 2000, PCCP, 2, 3401
Müller, H. S. P., Schlöder, F., Stutzki, J., & Winnewisser, G. 2005, JMoSt, 742, 215
Muñoz Caro, G. M., Meierhenrich, U. J., Schutte, W. A., Barbier, B., et al. 2002, Natur, 416, 403
Nummelin, A., Bergman, P., Hjalmarson, Å., et al. 2000, ApJS, 128, 213
Neill, J. L., Bergin, E. A., Lis, D. C., et al. 2014, ApJ, 789, 8
Öberg, K. I., Garrod, R. T., van Dishoeck, E. F., & Linnartz, H. 2009, A&A, 504, 891
Öberg, K. I., Bottinelli, S., Jørgensen, J. K., & van Dishoeck, E. F. 2010, ApJ, 716, 825
Öberg, K. I., van der Marel, N., Kristensen, L. E., & van Dishoeck, E. F. 2011, ApJ, 740, 14
Öberg, K. I., Lauck, T., & Graninger, D. 2014, ApJ, 788, 68
Ossenkopf, V., & Henning, T. 1994, A&A, 291, 943
Palau, A., Fuente, A., Girart, J. M., et al. 2011, ApJL, 743, L32
Parise, B., Ceccarelli, C., Tielens, A. G. G. M., et al. 2002, A&A, 393, 49
Parise, B., Ceccarelli, C., Tielens, A. G. G. M., et al. 2006, A&A, 453, 949
Pearson, J. C., Yu, S., & Drouin, B. J. 2012, JMoSp, 280, 119
Persson, M. V., Jørgensen, J. K., & van Dishoeck, E. F. 2012, A&A, 541, A39
Pickett, H. M., Poynter, R. L., Cohen, E. A., et al. 1998, JQSRT, 60, 883
Qin, S.-L., Wu, Y., Huang, M., et al. 2010, ApJ, 711, 399
Rodgers, S. D., & Charnley, S. B. 2001, ApJ, 546, 324
Schöier, F. L., Jørgensen, J. K., van Dishoeck, E. F., & Blake, G. A. 2002, A&A, 390, 1001
Taquet, V., Ceccarelli, C., & Kahane, C. 2012, A&A, 538, A42
Taquet, V., López-Sepulcre, A., Ceccarelli, C., et al. 2013, ApJL, 768, L29
Taquet, V., Charnley, S. B., & Sipilä, O. 2014, ApJ, 791, 1
Vastel, C., Ceccarelli, C., Lefloch, B., & Bachiller, R. 2014, ApJL, 795, L2
Wang, K.-S., Kuan, Y.-J., Liu, S.-Y., & Charnley, S. B. 2010, ApJ, 713, 1192
Wirström, E. S., Geppert, W. D., Hjalmarson, Å., et al. 2011, A&A, 533, A24
Xu, L.-H., & Lovas, F. J. 1997, JPCRD, 26, 17
Xu, L.-H., Fisher, J., Lees, R. M., et al. 2008, JMoSp, 251, 305
Zapata, L. A., Loinard, L., Rodríguez, L. F., et al. 2013, ApJL, 764, L14